

# Pushing the boundaries of asteroseismic individual frequency modelling: unveiling two evolved very low-metallicity red giants

J. R. Larsen<sup>1,\*</sup>, J. L. Rørsted<sup>1,2</sup>, V. Aguirre Børsen-Koch<sup>3</sup>, M. S. Lundkvist<sup>1</sup>, J. Christensen-Dalsgaard<sup>1</sup>, M. L. Winther<sup>1</sup>, A. Stokholm<sup>4,1</sup>, Y. Li<sup>5</sup>, D. Slumstrup<sup>6,7</sup>, H. Kjeldsen<sup>1,8</sup>, E. Corsaro<sup>9</sup>, O. Benomar<sup>10,11</sup>, S. Dhanpal<sup>12</sup>, A. Weiss<sup>13</sup>, B. Mosser<sup>14</sup>, S. Hekker<sup>15,16,1</sup>, D. Stello<sup>17,18,19,1</sup>, A. J. Korn<sup>20</sup>, A. Jendrieck<sup>21</sup>, Y. Elsworth<sup>4</sup>, R. Handberg<sup>1</sup>, T. Kallinger<sup>22</sup>, C. Jiang<sup>23</sup>, L. I. Mashonkina<sup>24</sup>, and G. Ruchti<sup>25,\*\*</sup>

<sup>1</sup> Stellar Astrophysics Centre (SAC), Department of Physics and Astronomy, Aarhus University, Ny Munkegade 120, 8000 Aarhus C, Denmark

<sup>2</sup> Aarhus Astronomy Data Centre (AADC), Department of Physics and Astronomy, Aarhus University, Ny Munkegade 120, 8000 Aarhus C, Denmark

<sup>3</sup> DARK, Niels Bohr Institute, University of Copenhagen, Jagtvej 128, 18, 2200, Copenhagen, Denmark

<sup>4</sup> School of Physics and Astronomy, University of Birmingham, Edgbaston B15 2TT, UK

<sup>5</sup> Institute for Astronomy, University of Hawai'i, 2680 Woodlawn Drive, Honolulu, HI 96822, USA

<sup>6</sup> European Southern Observatory, Alonso de Cordova 3107, Vitacura, Chile

<sup>7</sup> Instituto de Estudios Astrofísicos, Facultad de Ingeniería y Ciencias, Universidad Diego Portales, Ejército Libertador 441, Santiago, Chile

<sup>8</sup> Aarhus Space Centre (SpaCe), Department of Physics and Astronomy, Aarhus University, Ny Munkegade 120, 8000 Aarhus C, Denmark

<sup>9</sup> INAF – Osservatorio Astrofisico di Catania, Via S. Sofia, 78, 95123 Catania, Italy

<sup>10</sup> Department of Astronomical Science, School of Physical Sciences, SOKENDAI, 2-21-1 Osawa, Mitaka, Tokyo, 181-8588, Japan

<sup>11</sup> Solar Science Observatory, National Astronomical Observatory of Japan, 2-21-1 Osawa, Mitaka, Tokyo, 181-8588, Japan

<sup>12</sup> Scientific Machine Learning group, Rutherford Appleton Laboratory, Science and Technology Facilities Council, Harwell Campus, Didcot OX11 0QX, UK

<sup>13</sup> Max-Planck-Institute for Astrophysics, Karl-Schwarzschild-Str. 1, 85748 Garching, Germany

<sup>14</sup> LIRA, Observatoire de Paris, Université PSL, CNRS, Sorbonne Université, Université Paris-Cité, 92195 Meudon, France

<sup>15</sup> Heidelberger Institut für Theoretische Studien, Schloss-Wolfsbrunnenweg 35, 69118 Heidelberg, Germany

<sup>16</sup> Center for Astronomy (ZAH/LSW), Heidelberg University, Königstuhl 12, 69117 Heidelberg, Germany

<sup>17</sup> School of Physics, University of New South Wales, NSW 2052, Australia

<sup>18</sup> Sydney Institute for Astronomy (SIfA), School of Physics, University of Sydney, NSW 2006 Australia

<sup>19</sup> ARC Centre of Excellence for All Sky Astrophysics in 3 Dimensions (ASTRO 3D), Australia

<sup>20</sup> Division of Astronomy and Space Physics, Department of Physics and Astronomy, Uppsala University, Box 516, 75120 Uppsala, Sweden

<sup>21</sup> Independent Researcher, Munich, Germany – maxie.jendrieck@gmail.com

<sup>22</sup> Institut für Astrophysik, Universität Wien, Türkenschanzstrasse 17, 1180 Vienna, Austria

<sup>23</sup> Max-Planck-Institut für Sonnensystemforschung, Justus-von-Liebig-Weg 3, 37077 Göttingen, Germany

<sup>24</sup> Institute of Astronomy, Russian Academy of Sciences, Pyatnitskaya st. 48, 119017 Moscow, Russia

<sup>25</sup> Lund Observatory, Department of Astronomy and Theoretical Physics, Box 43, SE-221 00 Lund, Sweden

Received XXX, XXX; accepted XXX, XXX

## ABSTRACT

**Context.** Metal-poor stars play a crucial role in understanding the nature and evolution of the first stellar generation in the Galaxy. Previously, asteroseismic characterisation of red-giant stars has relied on constraints from the global asteroseismic parameters and not the full spectrum of individual oscillation modes. Using the latter, we present for the first time the characterisation of two evolved very metal-poor stars including the detail-rich mixed-mode patterns.

**Aims.** We will demonstrate that incorporating individual frequencies into grid-based modelling of red-giant stars enhances its precision, enabling detailed studies of these ancient stars and allowing us to infer the stellar properties of two very metal-poor [Fe/H]  $\sim -2.5$  dex *Kepler* stars: KIC 4671239 and KIC 7693833.

**Methods.** Recent developments in both observational and theoretical asteroseismology have allowed for detailed studies of the complex oscillation pattern of evolved giants. In this work, we employ *Kepler* time series and surface properties from high-resolution spectroscopic data within a grid-based modelling approach to asteroseismically characterise KIC 4671239 and KIC 7693833 using the Bayesian STellar Algorithm, BASTA.

**Results.** Both stars show agreement between constraints from seismic and classical observables; an overlap unrecoverable when purely considering the global asteroseismic parameters. KIC 4671239 and KIC 7693833 were determined to have masses of  $0.79_{-0.03}^{+0.04}$  and  $0.83_{-0.01}^{+0.03} M_{\odot}$  with ages of  $12.3_{-1.7}^{+1.7}$  and  $10.3_{-1.4}^{+0.6}$  Gyr, respectively. Particularly, for KIC 4671239 the rich spectrum of model frequencies closely matches the observed.

**Conclusions.** A discrepancy between the observed and modelled  $\nu_{\max}$  of  $\sim 9\%$  was found, indicating a metallicity dependence of the  $\nu_{\max}$  scaling relation. For metal-poor populations, this results in overestimations of the stellar masses and wrongful age inferences. Utilising the full spectra of individual oscillation modes lets us circumvent the dependence on the asteroseismic scaling relations through direct constraints on the stars themselves. This allows us to push the boundaries of state-of-the-art detailed modelling of evolved stars at metallicities far different from solar.

**Key words.** Asteroseismology – stars:individual – stars:oscillations – stars:interiors – stars:evolution

## 1. Introduction

The available archive of observed red-giant stars has been expanded significantly by the *Kepler* space mission (Borucki et al. 2010), allowing for many detailed studies to be carried out in its wake. These studies focus on the classification and understanding of red giants by the inferences possible from their oscillatory characteristics (e.g., Jiang & Christensen-Dalsgaard 2014; Mosser et al. 2018; Lindsay et al. 2022). The nature of these stellar pulsations is studied by the field of asteroseismology; the application of which has been revolutionised by the wealth of available time series data from *Kepler*. They allow for so-called seismic determinations of the fundamental stellar parameters such as mass, radius and surface gravity  $g$  – but importantly also the possibility of an accurate inference on the stellar age (see e.g. Soderblom 2015).

Until now, these seismic determinations of red giants have relied on extensive application of the asteroseismic scaling relations (Kjeldsen & Bedding 1995), which relate observed asteroseismic quantities other than the stellar masses and radii. The scaling relations are based on two global asteroseismic properties: the frequency of maximum oscillatory power  $\nu_{\max}$ , which is related to the surface gravity (Brown et al. 1991; Belkacem et al. 2011), and  $\Delta\nu$ , the average large frequency separation between consecutive modes of identical spherical degree  $\ell$ , owing a dependence to the mean density of the star (Tassoul 1980). The application of the asteroseismic scaling relations, known as the so-called *direct method* in the literature (for a review see Hekker 2020), entails that the inferences drawn carry the crucial assumption that we can scale the fundamental parameters of a star according to well-known solar values. In the asymptotic regime these relations are (Chaplin & Miglio 2013):

$$\Delta\nu \approx \left(\frac{M}{M_{\odot}}\right)^{1/2} \left(\frac{R}{R_{\odot}}\right)^{-3/2} \Delta\nu_{\odot} \quad (1)$$

$$\nu_{\max} \approx \left(\frac{M}{M_{\odot}}\right) \left(\frac{R}{R_{\odot}}\right)^{-2} \left(\frac{T_{\text{eff}}}{T_{\text{eff},\odot}}\right)^{-1/2} \nu_{\max,\odot} \propto \frac{g}{\sqrt{T_{\text{eff}}}}. \quad (2)$$

The benefit of applying Eqs. 1 and 2 is a model-independent determination of the stellar mass and radius if a measurement of the effective temperature  $T_{\text{eff}}$  is available. They have therefore been applied widely to *Kepler* red giants near solar metallicity. However, *Kepler* also discovered metal-poor giants. The application of the direct method for such stars was studied by Epstein et al. (2014) for a sample of nine metal-poor giants. Employing the scaling relations with effective temperatures from the Apache Point Observatory Galactic Evolution Experiment (APOGEE; Abdurro'uf et al. 2022), the authors found a systematic overestimation in the recovered masses compared to the expectation from e.g. fits to the colour-magnitude diagrams of globular clusters. The reliability of the scaling relations for red giants at compositions different than solar has therefore become questionable.

An alternative to the direct method is grid-based modelling, where the information on the composition can be incorporated by fitting the observed atmospheric and asteroseismic values to grids of stellar models. Thereby, theoretical values for the global asteroseismic parameters can be predicted from the models and compared to the observed counterparts (Stello et al. 2009; Silva Aguirre et al. 2015; Aguirre Børsen-Koch et al. 2022; Alencastro Puls et al. 2022; Huber et al. 2024). Matching the observed

values to the grids means that grid-based modelling has a critical dependence on our ability to infer accurate and reliable theoretical values of the atmospheric and global asteroseismic parameters for the stellar models. In case of  $\Delta\nu$  one can either employ Eq. 1 or obtain it from theoretically computed individual frequencies for the models. However, for  $\nu_{\max}$  the only option available for a theoretical estimate is to employ Eq. 2, where one may include several correction terms as a function of metallicity (e.g. Viani et al. 2017). The inability of estimating  $\nu_{\max}$  directly from the models stems from the stochastically excited nature of the oscillations themselves, where the non-adiabatic interplay between excitation (energy supplied from turbulent convection) and damping rate would be required to evaluate the amplitude of the oscillations (Houdek 2006).

In this work, for the first time within the field, the grid-based modelling of two evolved ( $\nu_{\max} \lesssim 100 \mu\text{Hz}$  as classified by Huber et al. 2024) red-giant stars will rely on fitting the complete range of  $\ell = 0, 1, 2$  observed individual frequencies, with the inclusion of the mixed modes. In red giants, any non-radial ( $\ell \neq 0$ ) individual frequencies will display mixed-mode characteristics. This occurs due to the unique possibility of a coupling between the interior g- and exterior p-mode properties, when the respective oscillation cavities exist at identical frequency ranges near  $\nu_{\max}$  (Jiang & Christensen-Dalsgaard 2014). The strength of the coupling is measured through the coupling constant  $q$ . The identification of such mixed modes means observing pressure modes that have been perturbed by the interior gravity-wave behaviour, thus carrying diagnostic information valuable for constraining the interior of the red-giant star. Modelling red giants through fitting directly to the individual frequencies will thereby circumvent the aforementioned dependence on the scaling relations; ideally providing the resulting stellar models whose interior profiles best match the constraints on the stellar interior supplied by the oscillation frequencies. This expansion was made possible by the recent developments of Larsen et al. (2024), allowing for the availability of the theoretical individual frequencies for red-giant stellar models in the context of large-scale grids.

Previously, Ball et al. (2018) employed a similar technique to fit the individual frequencies of three RGB stars, albeit with the goal of studying the surface effects for red giants. However, in their scheme they did not attempt to utilise the mixed modes of the models. This means that they had to match the observed frequencies to the single most p-mode-like model frequency (acoustic resonance) within each mode order. Hence, they lost the information on the deep stellar interior carried by the mixed modes and the asymptotic dipole mode period spacing  $\Delta\Pi_1$ . Recently, Huber et al. (2024) expanded the analysis by fitting the individual frequencies of a less evolved ( $\nu_{\max} \sim 200 \mu\text{Hz}$ ) metal-poor giant KIC 8144907, proving that stellar modelling of such stars is possible and, moreover, asteroseismically characterising the most metal-poor giant to date. In this work, we further extend the considerations and the approach of grid-based individual frequency modelling for similarly metal-poor, yet notably more evolved red giants with  $\nu_{\max} \lesssim 100 \mu\text{Hz}$ .

This project is the culmination of many years of efforts begun in the early 2010's, firstly by Jendrieck et al. (2012) and later led by V. Aguirre Børsen-Koch (formerly Silva Aguirre) and completed in the present work. The initial efforts focused on proper characterisation of two, to become notoriously vexing, very low-metallicity red-giant stars: KIC 4671239 (dubbed "Hennes") and KIC 7693833 (dubbed "Rogue"). These stars resisted proper and coherent characterisation in modelling efforts, and a thorough investigation effort was therefore undertaken to obtain atmospheric and asteroseismic determinations for both,

\* E-mail: jensrl@phys.au.dk

\*\* Greg sadly passed away before the completion of this manuscript. We acknowledge his contributions and extend our condolences to his family.

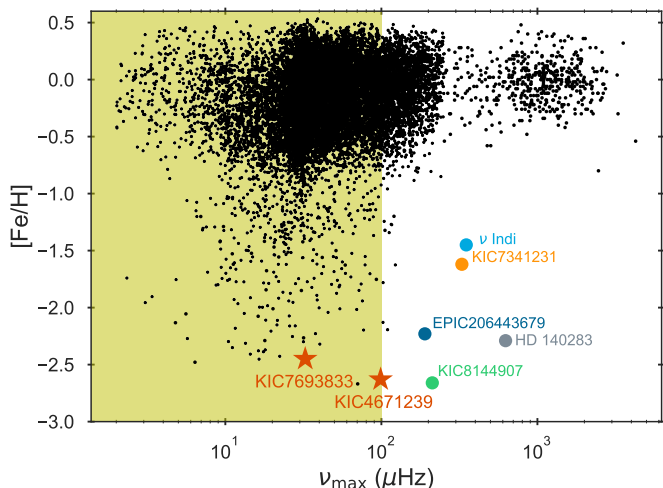


**Fig. 1.** Metallicity  $[Fe/H]$  plotted against the frequency of maximum oscillatory power  $\nu_{\max}$  for known oscillating stars, adapted from the left panel of Fig. 2 from Huber et al. (2024). The shaded area represents the region of evolved RGB stars, with a boundary set at  $\nu_{\max} \lesssim 100 \mu\text{Hz}$ . Noteworthy low-metallicity sub-giant branch (SGB) and RGB stars for which asteroseismic modelling has been performed are highlighted. Note that EPIC206443676 is modelled using the global asteroseismic parameters (Deheuvels et al. 2012), not the individual frequencies as in all other displayed cases. The red stars indicate the two giants considered in the present work.

before attempting to perform grid-based modelling. The project never reached completion and remained unpublished, primarily due to the lack of coherence between the fitted results and observational constraints. Additionally, both stars were recovered with solar-like ages, which conflicts with expectations from galactic archaeology that very low-metallicity (possibly halo) stars should be old. Our analysis includes various elements from the prior efforts by V. Silva Aguirre et al. (unpublished; in the following mentioned as A16).

KIC 4671239, henceforth Hennes, is one of the most metal-poor ( $[Fe/H] \sim -2.6$  dex) stars found in the *Kepler* field. As an individual star, Hennes has been studied several times in different contexts, first classified in the SAGA survey by Casagrande et al. (2014) using Strömgren photometry. Mosser et al. (2017) investigated the coupling factor  $q$  of mixed modes for red giants, and noted that specifically for Hennes it was found to be atypically high, resulting in a complex mixed-mode pattern. Furthermore, they determined a dipole spacing  $\Delta\Pi_1 \approx 66.6$  s – which characterises Hennes as a red-giant branch (RGB) star according to the work of Bedding et al. (2011) – that they note is much smaller than for other RGB stars of similar  $\Delta\nu$ . Hennes may then resemble stars identified by Deheuvels et al. (2022) as resulting from mass transfer, which would result in the inability of canonical stellar models describing the star. In this work, however, we find that the very low metallicity is the cause of the situation (see Sect. 6.3). An attempt to characterise Hennes using grid-based modelling with global asteroseismology, along with other giants, was performed by Alencastro Puls et al. (2022). They recovered a solar-like age for Hennes, and speculated the possibility for Hennes to be a blue straggler or potentially having experienced a merger event in its past. Recently, the ensemble study by Kuzlewicz et al. (2023) also recovered a high coupling factor  $q \sim 0.3$  for Hennes, proposing the possibility of high coupling values being an indicator of metal-poor giants.

KIC 7683833, hereafter Rogue, is a similarly metal-poor ( $[Fe/H] \sim -2.4$  dex) giant initially identified by Thygesen et al. (2012) and preliminarily studied by Jendrieck et al. (2012). Rogue has not been studied as an individual star since, but it has been classified by ensemble studies as an RGB star (Vrard et al. 2016; Elsworth et al. 2016; Mathur et al. 2017; Yu et al. 2018).

Fig. 1 is adapted from Huber et al. (2024)<sup>1</sup> and highlights the evolved nature of Hennes and Rogue alongside the extension to the previous situation that this work contributes. The shaded region represents evolved giants where individual frequency modelling is challenging to perform (see e.g, Fig 2 of Larsen et al. 2024). The small existing selection of asteroseismically modelled and characterised low- and very low-metallicity stars are seen in the figure, but all lie outside of the evolved region. Hennes and Rogue push into this region, extending the boundaries of individual frequency modelling, while also being the first very low-metallicity evolved red giants to be asteroseismically characterised.

The paper is structured as follows: in Sect. 2 we outline the spectroscopic and photometric observations of both stars, before continuing to the asteroseismic observations and reduction in Sect. 3. The details of the grid-based modelling is presented in Sect 4, with details on the stellar evolution and oscillation codes used. Furthermore, we briefly introduce the BAYesian STellar Algorithm (BASTA; Aguirre Børsen-Koch et al. (2022)) used within this work to perform the fitting. Section 5 presents the results obtained for Hennes and Rogue, before discussing their implications and further context in Sect. 6. Lastly, we conclude in Sect. 7.

## 2. Classical parameters

The various sources for the atmospheric and photometric parameters relevant for the modelling of Hennes and Rogue are outlined in the following. As mentioned in Sect. 1 there are estimations available for both stars from independent determinations. All literature values for the spectroscopic and photometric parameters of interest are listed in Table 1. The nuances and procedures for the estimates originating from this work will be presented below.

### 2.1. Atmospheric observations

The atmospheric analysis of A16 and repeated in this work was performed on observations taken at the Nordic Optical Telescope (NOT) in 2012/13. Both stars were observed with the FIES spectrograph, which is a fixed-setting spectrograph covering a spectral range of 370-730 nm without gaps (Telting et al. 2014). The observations were carried out with the medium-resolution setting, resulting in a resolving power of  $R = 46000$ . Hennes was observed on a single night in October 2013, obtaining four spectra of an hour each. Rogue was observed on two nights in August 2012, obtaining two spectra of an hour each. Additionally, for Rogue we obtained new high-resolution ( $R = 67000$ ) FIES spectra with a combined exposure time of  $\sim 4.8$  hours with the NOT in May 2024 in an effort to better characterise the star. The results marked "this work" in Table 1 for Rogue are obtained from these spectra, to be described below.

<sup>1</sup> The literature values that form the black points in the plot are from Pinsonneault et al. (2014), Serenelli et al. (2017), Matsuno et al. (2021) and Schonhut-Stasik et al. (2024).

**Table 1.** Compiled spectroscopic determinations for Hennes and Rogue from various sources. Note that the value for  $T_{\text{eff}}$  and  $[\text{Fe}/\text{H}]$  from Yu et al. (2018) for Hennes are adopted from Casagrande et al. (2014). For Rogue, Yu et al. (2018) adopted the corresponding values from Mathur et al. (2017), who in turn adopted them from Thygesen et al. (2012).

Source	$T_{\text{eff}}$ [K]	$\log(g)$	$[\text{Fe}/\text{H}]$ [dex]	$[\alpha/\text{Fe}]$ [dex]
<b>Hennes – KIC 4671239</b>				
Casagrande et al. (2014)	$5224 \pm 104$	$2.92 \pm 0.004$	$-2.44 \pm 0.17$	–
Yu et al. (2018)	$5224 \pm 100$	$2.922 \pm 0.006$	$-2.44 \pm 0.30$	–
Alencastro Puls et al. (2022)	$5295 \pm 145$	$2.929 \pm 0.15$	$-2.63 \pm 0.20$	$0.125 \pm 0.25$
Spect. 1, unpublished	$5175 \pm 150$	$2.50 \pm 0.15$	$-2.80 \pm 0.15$	–
Spect. 2, unpublished	$5407 \pm 150$	$2.91 \pm 0.15$	$-2.48 \pm 0.15$	–
This work	$5080 \pm 220$	$2.93 \pm 0.10$	$-2.71 \pm 0.11$	$0.12 \pm 0.16$
<b>Rogue – KIC 7693833</b>				
Thygesen et al. (2012)	$4880 \pm 100$	$2.46 \pm 0.01$	$-2.23 \pm 0.15$	–
Yu et al. (2018)	$4880 \pm 97$	$2.413 \pm 0.008$	$-2.23 \pm 0.15$	–
Abdurro'uf et al. (2022)	$5026 \pm 17.2$	$2.41 \pm 0.06$	$-2.33 \pm 0.01$	$0.34 \pm 0.10$
Spect. 1, unpublished	$5075 \pm 100$	$2.50 \pm 0.10$	$-2.37 \pm 0.10$	–
Spect. 2, unpublished	$5119 \pm 100$	$2.40 \pm 0.10$	$-2.20 \pm 0.10$	$0.3 \pm 0.1$
This work	$4840 \pm 150$	$2.43 \pm 0.10$	$-2.45 \pm 0.05$	$0.15 \pm 0.12$

A16 carried out two unpublished spectroscopic analyses for each star, denoted "Spect. 1" and "Spect. 2", using the 2012/13 NOT spectra. Both approaches used an iterative process to determine the stellar parameters. The effective temperature was determined from the self-broadened wings of  $H\alpha$  in both cases. Spect. 1 includes NLTE corrections for  $H\alpha$ , while Spect. 2 additionally employs the colour-excitation temperature calibration described in Ruchti et al. (2011). The surface gravity and metallicity were determined from the ionisation balance of Fe lines in NLTE using spectral synthesis in Spect. 1 (Mashonkina et al. 2011) and equivalent width measurements in Spect. 2 (Ruchti et al. 2013). The microturbulent velocity was set by minimising the slope in the relationship between iron abundance and line strength using weak and moderately strong lines of both ionisation stages. The results of these two methods carried out by A16 are listed in Table 1. They serve as comparisons for the current investigations.

For the present work the spectroscopic analysis follows the method outlined in Slumstrup et al. (2019) by using the asteroseismically determined surface gravity to constrain a classical equivalent width analysis of Fe lines. The effective temperature is varied until excitation equilibrium is reached, i.e. no trend is observed between the abundance and the excitation potential of the Fe lines. Likewise, the microturbulence is determined by removing the trend between the abundance and the strength of the Fe lines. Uncertainties were calculated by varying each parameter until at least a  $3\sigma$  uncertainty is produced on the slope of  $[\text{Fe}/\text{H}]$  vs. excitation potential. Agreement between abundances of FeI and FeII lines to within one standard deviation was assured throughout the analysis. The equivalent widths were measured with DAOSPEC (Stetson & Pancino 2008) and the abundances were calculated with the auxiliary program *Abundance* with SPECTRUM in LTE (Gray & Corbally 1994). The stellar atmosphere models used are ATLAS9 (Castelli & Kurucz 2004) with solar abundances from Grevesse & Sauval (1998). The stars analysed in the present work are significantly more metal-poor than those of Slumstrup et al. (2019) and therefore it has been necessary to implement NLTE departure-coefficients taken from the INSPECT database version 1.0<sup>2</sup> (Bergemann et al. 2012; Lind et al. 2012).

The metallicities  $[\text{Fe}/\text{H}]$  derived in this work are on average lower than the alternative measurements. However, this is in coherence with expectations as the derived temperatures are also lower. In this parameter space, a lower temperature will provide stronger spectral lines, effectively cancelling out the effect of a lower metallicity. Conversely, in the other estimates the temperatures and metallicities are higher, once again counteracting each other and giving coherent results. The determining factor then becomes the microturbulence as a fitting parameter, which becomes difficult to implement in this very low-metallicity regime for a 1D NLTE approach.

In the case of Hennes, the choice of spectroscopy required additional considerations. The choice was between our own contemporary results from the NOT observations of 2013 and the results of Alencastro Puls et al. (2022) from the HIRES spectrograph (Vogt et al. 1994). The two datasets are consistent within the uncertainties, yet when comparing to purely spectroscopic test-fits to stellar atmospheric models, a self-consistent overlap between all parameters and the models only occur for the HIRES spectroscopy of Alencastro Puls et al. (2022). Furthermore, HIRES is mounted on the larger W. M. Keck telescope and the observations have a higher signal-to-noise ratio than the NOT counterparts for Hennes. We therefore choose to employ the spectroscopic determinations of Alencastro Puls et al. (2022). The estimate of the alpha-enhancement  $[\alpha/\text{Fe}]$  is calculated as the mean of the two alpha-element abundances from magnesium and calcium, with the uncertainty found by adding the individual element uncertainties in quadrature.

For Rogue we choose to use the spectroscopic determination from our contemporary work. They are consistent with the other estimates within the uncertainties. As argued above, the differences seen in Table 1 are likely caused by the difficult parameter space of the star for 1D NLTE approaches, and indicates that both stars would likely benefit from a full 3D NLTE analysis in the future.

## 2.2. Photometric and astrometric observations

In order to obtain constraints on the stellar luminosities (see Aguirre Børsen-Koch et al. 2022 for details), we need a measure for the parallax and observed magnitudes. In *Gaia* DR3 (Gaia Collaboration et al. 2016, 2023), the 5-parameter astrometric so-

<sup>2</sup> Available at [www.inspect-stars.com](http://www.inspect-stars.com)

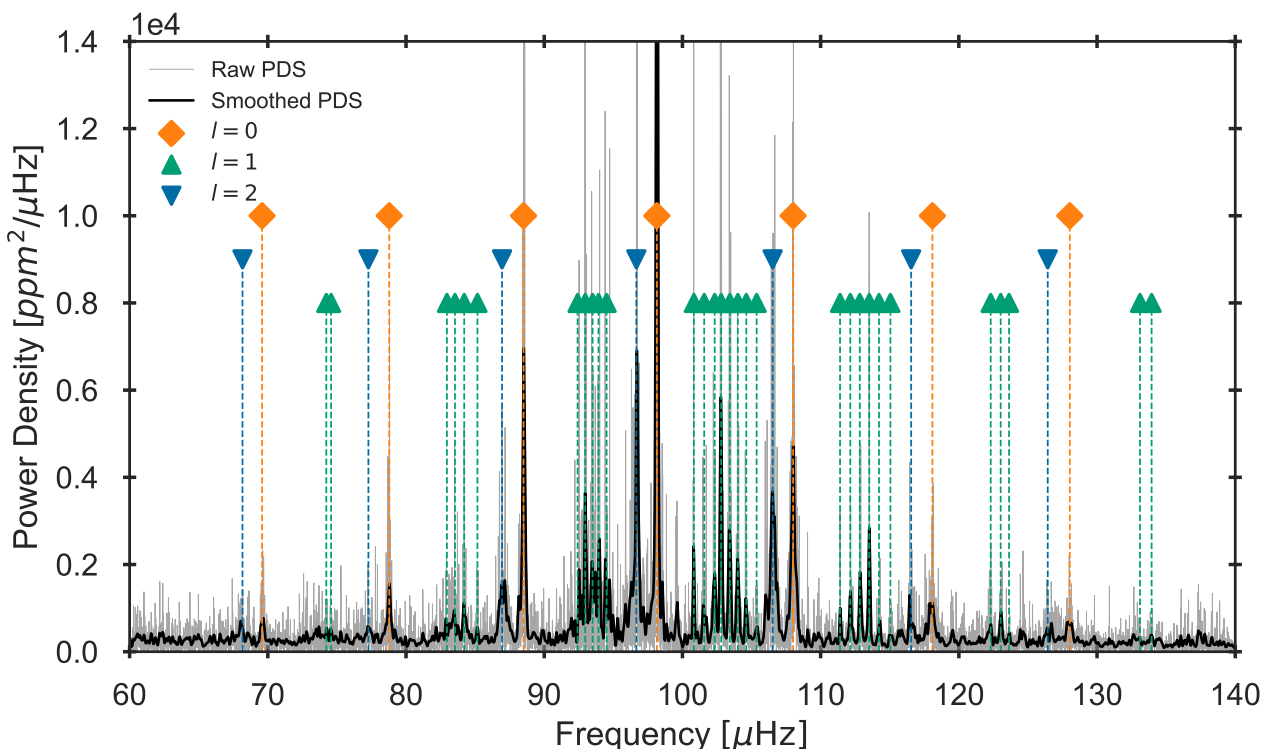


**Fig. 2.** Power density spectrum of Hennes with the consolidated list of individual frequencies from Table A.2 overlaid. Both the raw spectrum (shaded gray) and a Gaussian smoothed version (black) are seen. The orange diamonds, green upwards and blue downwards triangles depict the  $\ell = 0$ ,  $\ell = 1$  and  $\ell = 2$  modes, respectively.

lution was measured for both Hennes and Rogue as well as the *Gaia*  $G$ ,  $G_{BP}$ , and  $G_{RP}$  magnitudes, hence we can add these to the inference of stellar properties. Hennes has a magnitude of 13.6 in the G band, while Rogue has a magnitude of 11.7. The uncertainties of the *Gaia* magnitudes are internal and extremely small. A floor of  $\sigma = 0.01$  has therefore been set for all magnitudes retrieved. The *Gaia* parallaxes were also recovered and have been corrected for their known zero-point error according to the description of Lindegren et al. (2021). This results in a corrected parallax of 0.471 and 0.659 mas for Hennes and Rogue, respectively.

### 3. Asteroseismic observations and data reduction

Hennes and Rogue were observed in the nominal *Kepler* mission. The time series were recovered from the KASOC database<sup>3</sup> after reduction by the pipeline (Handberg & Lund 2014). Subsequently, they were reduced to form the power density spectra (PDS) of both stars following the prescription by Handberg & Campante (2011a). Several independent analyses of the PDS were performed, providing primarily the observed individual frequencies for comparison and cross-referencing. Depending on the analysis employed, estimates of the global asteroseismic parameters were also returned. The nuances of the independent determinations and their results are described in Appendix A, where Table A.1 summarises the global asteroseismic parameter estimates obtained. Subsequently, we briefly describe the procedure for obtaining the global asteroseismic parameters in this work.

The value of  $\nu_{\max}$  was found by assuming that the power excess represents a Gaussian envelope (Bedding 2014), where the

vertex defines  $\nu_{\max}$ . Repeatedly applying a Gaussian smoothing with a large standard deviation to the PDS allows for the production of the envelope and the subsequent retrieval of  $\nu_{\max}$  for each of the stars. The uncertainty was estimated by varying the length of the time series that formed the PDS and changing the width of the Gaussian, meanwhile recording the variations in the derived value for  $\nu_{\max}$ . These estimates agree with those outlined in Appendix A.

For  $\Delta\nu$  we apply the method of autocorrelation to recover the periodicity stemming from the even spacing in frequency of the p-modes in the PDS. From the autocorrelation function<sup>4</sup>, the peaks corresponding to multiples of  $\Delta\nu$  are extracted and a linear correlation through the origin is fitted. The gradient of this linear fit provides  $\Delta\nu$  with the uncertainty estimated from the associated covariance matrix. Once more, the values of  $\Delta\nu$  obtained corresponds well with the other independent determinations.

The dipole period spacing  $\Delta\Pi_1$  was determined by A16 by employing a de-convolution of the gravity-mode pattern from the mixed-mode pattern (Mosser et al. 2015), which takes into account the signature of a buoyancy glitch (Cunha et al. 2015; Lindsay et al. 2022; Cunha et al. 2024). This framework works for Hennes, and returns a value consistent with the independent determinations. Due to the more evolved nature of Rogue, the proximity between the observed dipole modes exceeds the frequency resolution of the PDS. This, in combination with a weak coupling due to a small coupling factor  $q$  (see Sect. 3.2), makes the determination of the dipolar period spacing  $\Delta\Pi_1$  very uncertain.

<sup>4</sup> Calculated with the STATS MODELS module ACF <https://www.statsmodels.org/stable/generated/statsmodels.tsa.stattools.acf.html>.

<sup>3</sup> <https://kasoc.phys.au.dk>

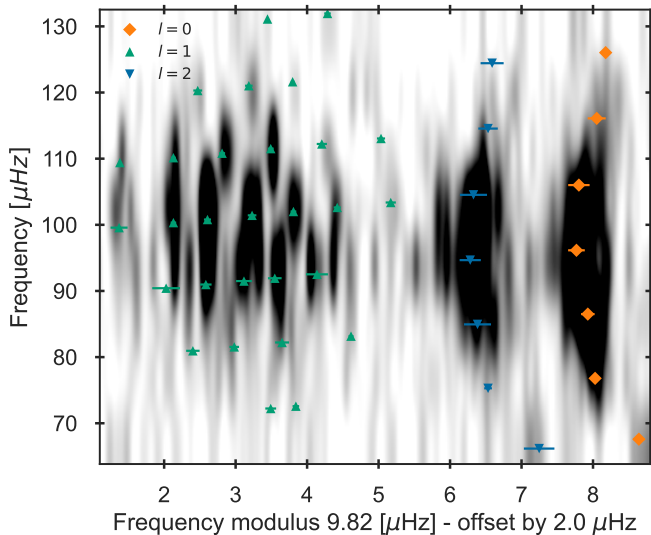


**Fig. 3.** Observed power échelle diagram for Hennes with the consolidated list of individual frequencies from Table A.2 overplotted. The orange diamonds, green upwards and blue downwards triangles depict the  $\ell = 0$ ,  $\ell = 1$  and  $\ell = 2$  modes, respectively.

Subsequently, we summarise the obtained parameters for each star and the inferences possible, before presenting the observed individual frequencies.

### 3.1. Hennes - KIC 4671239

**Table 2.** Global asteroseismic parameters for Hennes (KIC 4671239) and Rogue (KIC 7693833).

Global parameter	Hennes	Rogue
$\nu_{\max}$ [ $\mu\text{Hz}$ ]	$98.9 \pm 1.2$	$32.5 \pm 0.2$
$\Delta\nu$ [ $\mu\text{Hz}$ ]	$9.82 \pm 0.05$	$3.98 \pm 0.01$
$\Delta\Pi_1$ [s]	$66.0 \pm 1.0$	$56.6 \pm 2.0$

Hennes was observed by *Kepler* from Q1-Q17 in long-cadence mode, with Q6, Q10 and Q14 missing due to the failing of CCD module 3. The resulting timeseries with a length of  $\sim 3.5$  years produces the PDS seen in Fig. 2. In this PDS, the dipole mixed modes are clearly separated at higher frequency. This is a result of the unusually high coupling factor of  $q = 0.26 \pm 0.03$  found for Hennes, which reflects a small evanescent region in its interior resulting in a strong perturbation to the p-modes by the g-modes (see Sect. 6.3 for a discussion on these aspects). Furthermore, it indicates the less evolved nature of Hennes, where the radiative dampening is not yet strong enough to damp the strongly coupled dipole mixed-modes (Grosjean et al. 2014). We note that one of the independent determinations returned an estimated inclination of  $57 \pm 2$  degrees, which could enforce the possibility of rotational splitting of the modes, tentatively observed for some quadrupole modes in the PDS. Table 2 presents the values obtained for the global asteroseismic parameters of Hennes. The star is thus right past the border to being an evolved RGB star (cf. Fig. 1), confirmed by both the value of  $\Delta\nu$  and  $\Delta\Pi_1$  (Bedding et al. 2011).

The individual frequencies obtained from all independent determinations for Hennes were manually inspected and compared. The frequencies recovered from the FAMED pipeline (Corsaro

et al. 2020) were chosen as they show the most conservative fit to the observed power in the PDS. A cross-match was then performed to only accept frequencies which depicted an overlap within  $2\sigma$  to the corresponding mode in another set of determinations. The consolidated list of frequencies are displayed in Table A.2 and show 7 detected acoustic orders, with an additional isolated quadrupole mode at low frequency. This consolidated list was later validated by comparing to the results of the TACO code by Hekker et al. in prep (see Appendix A.4). Figure 2 shows the frequencies overplotted on the PDS, while Fig. 3 displays the modes in an observed power échelle diagram. An échelle diagram uses the even spacing in frequency of the p-modes to stack the PDS vertically in units of  $\Delta\nu$ . In Fig. 3, the observed power is plotted in a binned grid to allow for visible inspection of the frequency determinations, which should depict a clear overlap with the power. Figure 3 clearly illustrates the evolved mixed-mode pattern of Hennes, where a broad selection of dipole modes have been identified across various mode orders. When using the determined frequencies in Table A.2 for the inference in Sect. 5, we apply a correction to the Doppler-shift stemming from the radial velocity  $V_r$  of the star as discussed by Davies et al. (2014). This correction factor is calculated for Hennes to be  $1 + V_r/c = 0.99937$ , where  $c$  is the speed of light and  $V_r$  is  $-189.38$  km/s obtained from Gaia DR3 data.

### 3.2. Rogue - KIC 7693833

Rogue was observed through Q0-Q17 in long-cadence mode; the entire nominal mission of *Kepler*, providing a 4-year long timeseries from which the PDS in Fig. 4 is produced. Worth noting is the broadened and substantial power clusters attributed to the dipole modes. In contrast to individual dipole frequency peaks, these clusters arise due to the smaller period spacing and lower coupling strength for this more evolved star; two independent determinations find it to be  $q \lesssim 0.09$  (see Table A.1; Dhanpal et al. 2022). The enhances mixing is due to the evolved nature of Rogue, as the oscillation spectrum becomes increasingly dense with evolution (Mosser et al. 2018; Larsen et al. 2024). Furthermore, this results in a slight rightwards shift of the dipole modes from the central position between the  $\ell = 0$  and  $\ell = 2$  peaks, as expected from the considerations by Bedding et al. (2010) and Stello et al. (2014).

As shown in Table 2, the values of  $\Delta\nu$  and  $\nu_{\max}$  determined for Rogue indicate an RGB star further evolved compared to Hennes, likely situated just prior to the location of the RGB bump (Khan et al. 2018). The dipole period spacing was determined to be  $\sim 56 \pm 2$  s. However, as introduced earlier, this determination is very uncertain due to the nature of Rogue. The independent determinations found values ranging from 61 to 105 seconds, with uncertainties as large as 58 seconds. Bearing this in mind, the later modelling of Rogue is unable to consider the period spacing as a global parameter for fitting in Appendix C.

The individual frequencies recovered by the approach of Li et al. (2020) were selected for Rogue, as the determination of the radial ( $\ell = 0$ ) and quadrupole ( $\ell = 2$ ) modes overlap with all other independent determinations. Furthermore, the frequency set includes only the single p-dominated dipole mode in each mode order. This is desirable, as the reliability of the dipole mixed-mode determination is questionable for Rogue due to the concerns outlined above regarding the frequency resolution and the low coupling factor. The list of determined frequencies is provided in Table A.3 and shows 5 fully detected acoustic orders with two additional isolated modes, one radial and

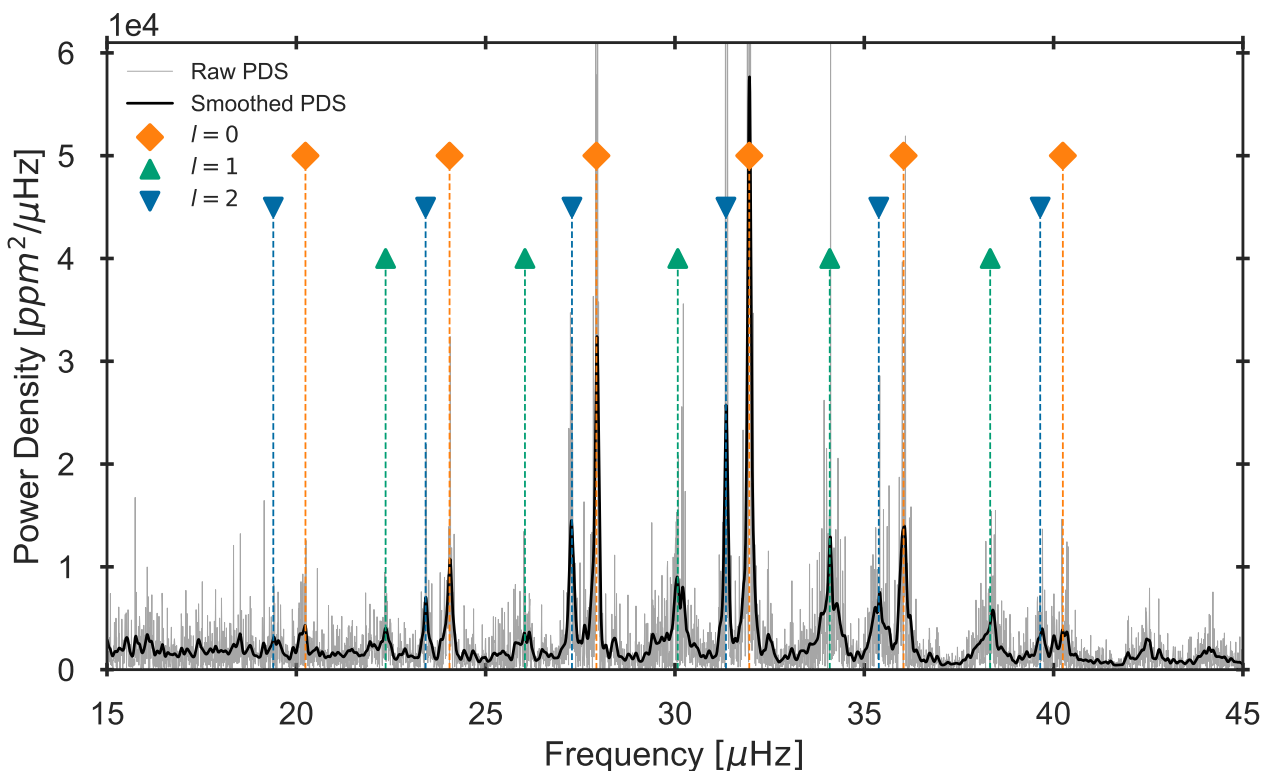


**Fig. 4.** Power density spectrum of Rogue with the consolidated list of individual frequencies from Table A.3 overplotted. Both the raw spectrum and a Gaussian smoothed version are shown as the shaded gray and black spectra, respectively. The orange diamonds, green upwards and blue downwards triangles depict the  $\ell = 0$ ,  $\ell = 1$  and  $\ell = 2$  modes, respectively.

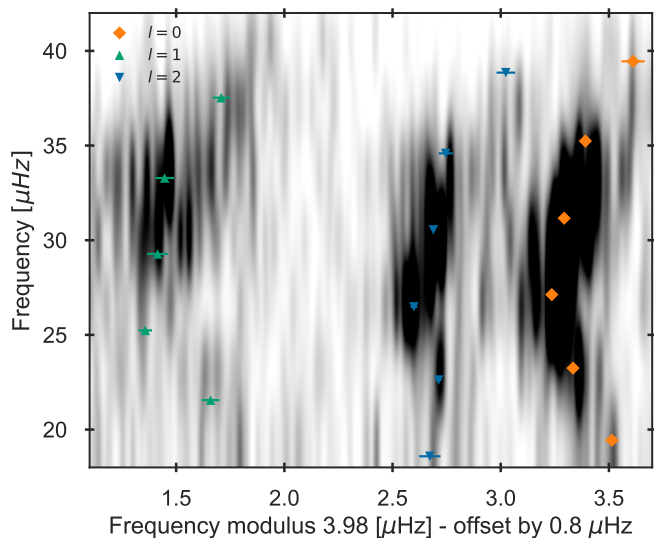


**Fig. 5.** Observed power échelle diagram for Rogue with the consolidated list of individual frequencies from Table A.3 overplotted. The orange diamonds, green upwards and blue downwards triangles depict the  $\ell = 0$ ,  $\ell = 1$  and  $\ell = 2$  modes, respectively.

one quadrupole. This consolidated list was also cross-checked against the results of TACO for validation.

The fitting of  $\ell = 2$  modes as Lorentzian profiles is under the assumption that they originate from a damped oscillator. This may pose issues due to the presence of mixed modes. Mixed modes can lead the fitting process to converge on a spe-

cific mixed mode instead of a pure p-mode. This misidentification can result in a smaller line width and an unrealistically low frequency uncertainty. Kjeldsen & Bedding (2012) proposed that frequency uncertainty scales with  $\sqrt{T^2 + \tau^2}$ , where  $T$  is the time series duration and  $\tau$  is the mode lifetime. The mode lifetime  $\tau$  is related to the linewidth  $\Gamma$  by  $\tau = (\pi\Gamma)^{-1}$ .

In principle, the linewidth of oscillation modes should vary smoothly as a function of frequency (Appourchaux et al. 2014; Lund et al. 2017). Let us consider fitting an  $\ell = 2$  mode with a linewidth  $\Gamma_2$ , and an adjacent  $\ell = 0$  mode with a linewidth  $\Gamma_0$ . If the result shows  $\Gamma_2 < \Gamma_0$ , this discrepancy may indicate the fitting issue described earlier. To address this, we inflated the uncertainty of the  $\ell = 2$  mode frequency by a factor of  $\sqrt{T^{-2} + (\pi\Gamma_0)^2} / \sqrt{T^{-2} + (\pi\Gamma_2)^2}$ .

Figure 4 shows the modes overplotted on the PDS, while Fig. 5 indicates the modes in an échelle diagram. As we consider a substantially evolved red giant, a departure in the power distribution from the approximately vertical ridges is seen. Similarly to Hennes, the frequencies displayed in Table A.3 are corrected when input to BASTA. For Rogue, the correction factor is  $1 + V_r/c = 0.99998$ , based on a  $V_r$  of  $-6.86$  km/s.

#### 4. Grid-based modelling of red giants

The modelling of our two red giants will follow the grid-based modelling approach. Stellar modelling involves many sources of degeneracy between various input parameters (see Basu & Chaplin 2017 for a review). This poses a challenge for so-called forward modelling, where models are iteratively calculated to match the observations. In this scheme, proper exploration of high-dimensional parameter spaces can become chal-

lenging, leading to issues stemming from the unresolved degeneracies. The grid-based method avoids this problem by trading it for a computationally expensive approach through the formation of large-scale grids of stellar models. Traditionally, the grid-based modelling approach was applied to examine suites of numerous stars using the same grid, without the need for recalculating the models. Here, we choose to employ the grid-based modelling for in-depth single-star studies (see e.g., Stokholm et al. 2019; Winther et al. 2023), warranted by the challenging metal-poor and evolved nature of Hennes and Rogue. The production of representative grids for each of the stars in question is costly in terms of computational resources. Yet, it is critical that they contain stellar models that appropriately span the suitable and often wide parameter space, as it provides insight into the degeneracies in and tentative solutions of the modelling.

The stellar evolution models in this work are computed using GARSTEC (Weiss & Schlattl 2008). The equation of state employed in the code originates from the OPAL group (Rogers et al. 1996; Rogers & Nayfonov 2002) and augmented in the low temperature end by that of Mihalas-Hummer-Däppen (Däppen et al. 1988; Hummer & Mihalas 1988; Mihalas et al. 1988; Mihalas et al. 1990). The treatment of atomic diffusion follows the prescription by Thoul et al. (1994). Various compilations for the opacities are used. For high temperatures it is the ones from OPAL (Rogers & Iglesias 1992; Iglesias & Rogers 1996), while for low temperature the opacities from Ferguson et al. (2005) are used. The nuclear reaction rate cross-sections originate from NACRE (Angulo et al. 1999), except for the reactions  $^{14}\text{N}(p, \gamma)^{15}\text{O}$  and  $^{12}\text{C}(\alpha, \gamma)^{16}\text{O}$  which are from Formicola et al. (2004) and Hammer et al. (2005), respectively. As both of our stars have low metallicity, there is a possibility of them being  $\alpha$ -enhanced, as confirmed by the spectroscopic determinations in Table 1. The stellar abundances used were chosen to be from Asplund et al. (2009), for which versions varying the degree of  $\alpha$ -enhancement  $[\alpha/\text{Fe}]$  in steps of 0.1 dex were calculated. When calculating the synthetic magnitudes of the models, the bolometric corrections by Hidalgo et al. (2018) were used.

#### 4.1. Tailored grids of stellar models

Carrying out detailed grid-based modelling for Hennes and Rogue entails producing stellar grids for each star. The grids are formed by a local grid-building routine<sup>5</sup> which samples the defined parameter space of initial parameters, e.g.  $M_{\text{ini}}$ , according to a quasi-random Sobol sampling (Sobol & Levithan 1976; Sobol 1977; Antonov & Saleev 1980; Fox 1986; Bratley & Fox 1988; Joe & Kuo 2003). In setting up these grids, only models on the RGB are included as Hennes and Rogue are in this evolutionary state (see Sects. 1 and 3). However, we also performed initial tests using a wider grid containing tracks evolved through the helium flash and onto the core helium burning phase from Borre et al. (2022). In these tests, we fit the same observables as for the modelling results of Hennes and Rogue presented in Sect. 5, however only the radial mode frequencies were taken into account. The test results confirmed RGB membership, with no likely solutions among post-RGB models. Furthermore, these initial tests provide a rough estimate of the suitable parameter space for each star.

The evolutionary region where models are recorded is defined by an interval in  $\Delta\nu$ , the value of which decreases with evolutionary stage. The models are evolved from the pre-main sequence until a certain  $\Delta\nu$  (the lower bounds in Table 3). The

**Table 3.** The parameter space with the varied dimensions of the tailored grids for Hennes and Rogue.

Hennes – KIC 4671239		
Stellar parameter	Lower bound	Upper bound
$M [M_{\odot}]$	0.70	1.00
$[\text{Fe}/\text{H}] [\text{dex}]$	-3.0	-2.2
$f_{\text{ov}}$	0	0.032
$\eta$	0	0.25
$[\alpha/\text{Fe}] [\text{dex}]$	0	0.5
$\Delta\nu [\mu\text{Hz}]$	16	7
Rogue – KIC 7693833		
Stellar parameter	Lower bound	Upper bound
$M [M_{\odot}]$	0.8	1.05
$[\text{Fe}/\text{H}] [\text{dex}]$	-2.65	-2.25
$f_{\text{ov}}$	0	0.02
$\alpha_{\text{mlt}}$	1.5	2.00
$Y_{\text{ini}}$	0.246	0.280
$[\alpha/\text{Fe}] [\text{dex}]$	0	0.4
$\Delta\nu [\mu\text{Hz}]$	5.5	2.5

evolution in GARSTEC is then halted and diagnostic checks are performed, before the calculations are restarted with models being recorded until arriving at the value of  $\Delta\nu$  indicated by the upper bound in Table 3. An overarching prior on the stellar models is a maximum age of 20 Gyr, for which the calculations are stopped for the given track if reached.

##### 4.1.1. Hennes – KIC4671239

The tailored grid for Hennes consists of 2500 stellar tracks. The boundaries of the spanned parameter space are listed in Table 3. The parameter space is firstly defined by the stellar mass and metallicity, for which wide boundaries are used. The convective overshooting efficiency  $f_{\text{ov}}$  according to the exponential scheme of Freytag et al. (1996) is varied from zero to twice the maximal value found through fits to globular clusters (Hjørringgaard et al. 2017). Mass loss is also included in the grid, varying the efficiency parameter  $\eta$  according to the prescription by Reimers (1977). The  $\alpha$ -enhancement is sampled from 0 to 0.5 dex. For this grid, the mixing-length parameter was set according to the mixing-length description by Kippenhahn et al. (2013) to a solar calibrated value of  $\alpha_{\text{mlt}} = 1.786$ . The initial helium abundance is set by a chemical enrichment law with  $dY/dZ = 1.4$  (Balsler 2006; Brogaard et al. 2012).

##### 4.1.2. Rogue – KIC7693833

The tailored grid for Rogue is considerably larger than for Hennes, consisting of 8192 stellar tracks. The initial test-fitting of Rogue produced a discrepancy between the observed and modelled temperature of the star. Additionally, the overlap with the magnitudes was at times poor. Lastly, Rogue initially indicated a tentative higher mass solution. The combination of these aspects warranted a larger and more exhaustive grid for Rogue.

A key inclusion was to allow the mixing length parameter  $\alpha_{\text{mlt}}$  and initial helium abundance  $Y_{\text{ini}}$  to vary freely. A change in the mixing length can cause differences in  $T_{\text{eff}}$  of  $\sim 100$  K on the RGB (Cassisi 2017; Tayar et al. 2017). It was thus sampled in a wide range from 1.5 to 2.0. Altering  $Y_{\text{ini}}$  will affect the luminosity of the models. However, models with  $Y_{\text{ini}}$  below the Big Bang nucleosynthesis value may sometimes provide

<sup>5</sup> Named AUBuild; planned for eventual public release

a better fit when considering individual frequencies. As such, we allow for the lower bound to be slightly below this value of  $Y_p = 0.24672 \pm 0.00017$  (Planck Collaboration et al. 2016; Pitrou et al. 2018; Cooke & Fumagalli 2018). This will allow us to check for this tentative situation and add priors subsequently if needed. To account for the higher dimensionality of the parameter space, it was decided to disregard the effect of mass-loss for this grid, as it was found to be negligible for Hennes and likely would have little effect despite the more evolved nature. Furthermore, to ensure proper resolution we reduce the upper bound for the convective overshooting efficiency  $f_{ov}$ .

#### 4.1.3. Pulsation code and model frequencies

The individual oscillation frequencies for all models in the grids were computed with the Aarhus Adiabatic Pulsation Package (ADIPLS; Christensen-Dalsgaard 2008, version 0.4). Importantly, the extension developed by Larsen et al. (2024) was implemented. This allows for efficient computation of the individual frequencies in the observable intervals for each model. Previously, the derivation of the individual frequencies for RGB models was only possible when performing forward-modelling, for which the frequencies could be computed for the few best-fitting models. Here, for the first time in context of grid-based modelling, the mixed modes of the individual frequencies are available for all stellar models before the fitting is performed.

This difference enables us to estimate  $\Delta\nu$  for the stellar models according to the individual frequencies instead of Eq. 1. Furthermore, it will allow for the fitting of the observed mixed-mode frequencies of Hennes and Rogue to the grids, which is a crucial extension to prior modelling efforts of evolved red giants.

#### 4.2. Fitting observations to models

The fitting algorithm used to match observations to models is the Bayesian STellar Algorithm (BASTA; Aguirre Børsen-Koch et al. 2022). It relies on Bayesian inference to infer a set of model properties given the provided observables. It does so through Bayes' theorem, which allows for the combination of prior knowledge on the stellar parameters  $\Theta$  with the data  $\mathbf{D}$  to yield the likelihood  $P(\mathbf{D}|\Theta)$  of observing the data given the model parameters. For specific details see Aguirre Børsen-Koch et al. (2022). The resulting product from BASTA is a marginalised posterior distribution readily available for inspection. It can be multimodal, meaning it can display more than a single solution for given stellar parameters. As such, it is important to verify the posterior after running the fitting routines. The preferred solution for each parameter is given as the median of the posterior, with uncertainties obtained from the credibility interval formed by the 16th and 84th percentiles of the distribution. Importantly, BASTA is a versatile algorithm that allows for various different observables to be fitted in combination, enabling the detailed modelling that our two stars require.

##### 4.2.1. Fitting individual frequencies

The fitting of the individual frequencies follows the default algorithm within BASTA. This consists of two steps for each model. Firstly, given the abundance of mixed modes in the models, the matching of observed modes to modes in the model is performed. This is done using the standard method in BASTA (Aguirre Børsen-Koch et al. 2022, Stokholm et al. in prep), with subtle adjustments for application to red-giant stars. Secondly,

after identifying the matching  $\ell = 0, 1, 2$  model frequencies, they are corrected using the surface correction of Ball & Gizon (2014) using only the cubic term. We choose to use only the cubic term as we fit a modest number of modes for Rogue, which means we are unable to properly constrain the inverse term of Ball & Gizon (2014) and risk overfitting. We note, however, that the posteriors remain unchanged when using the complete formulation.

There exist previous studies on the application of this surface correction on the RGB, which mention an over-correction issue due to the inertia scaling (Li et al. 2018; Ball et al. 2018). The application of the surface correction may result in the non-radial mixed modes being out of order, i.e. the monotonic relationship between mode order and frequency of the theoretical frequencies is broken. This is because the surface correction shifts an acoustic resonance beyond the adjacent oscillations due to its comparably lower inertia. Matching the observed mixed modes to the surface corrected frequencies would thus mean potentially matching to an unphysical representation of the oscillation spectrum. We avoid this as the matching in BASTA is performed before application of the surface correction. Subsequently, when the surface correction is applied, we find that the effect described in Ball et al. (2018) impacts the models in the grid for Rogue. Yet, due to the order of the matching procedure, it will not change the statistics of the performed fitting. A discussion regarding the performance of the frequency matching algorithm can be found in Sect. 6.1.

## 5. Results of asteroseismic modelling

The modelling of Hennes and Rogue was extensively explored and included a variety of different fitting cases and consistency tests. In the following, for the sake of brevity and clarity, we present only the case that represents the key extension to prior efforts that this work contributes: the fitting of the individual frequencies. As will become clear, this case is the only approach that yields self-consistent results and provide proper overlap between the constraints from the observables. We thus fit the individual frequencies for Hennes and Rogue in Tables A.2 and A.3, respectively. In addition the fits included the observed spectroscopic parameters  $T_{\text{eff}}$ ,  $[\text{Fe}/\text{H}]$  and  $[\alpha/\text{Fe}]$  along with the distance through the combination of parallax with the *Gaia* G, BP and RP magnitudes.

### 5.1. Hennes – KIC4671239

The results for Hennes are displayed in Table 4, compared with the results of A16 and Alencastro Puls et al. (2022). For inspection of the posteriors, see Fig B.1. The detailed asteroseismic modelling with tailored grids and individual frequencies in this work has solved the tension of prior results displaying a low stellar age (presented in Sect. 1). Hennes being a metal-poor halo star (see Sect. 6.4) is now classified as a low-mass high-age star, in coherence with expectations.

Figure 6 show the fit of the individual frequencies in a replicated échelle diagram. The fit to the individual frequencies is satisfactory and shows a best-fitting model with a mixed mode pattern matching that of Hennes very closely. Fitting the dipole mixed-modes directly allows us to capture the underlying period spacing of the model, clearly seen in the most populated mode orders in Fig. 6. The resulting prediction of  $\Delta\Pi_1$  from the fit is also consistent with the observed value. The modelled  $\Delta\nu$  value is slightly smaller than the observed. This is due to the fact that the  $\Delta\nu$  in the models is based on the radial frequencies only, which does not match well with the asymptotic relation for this

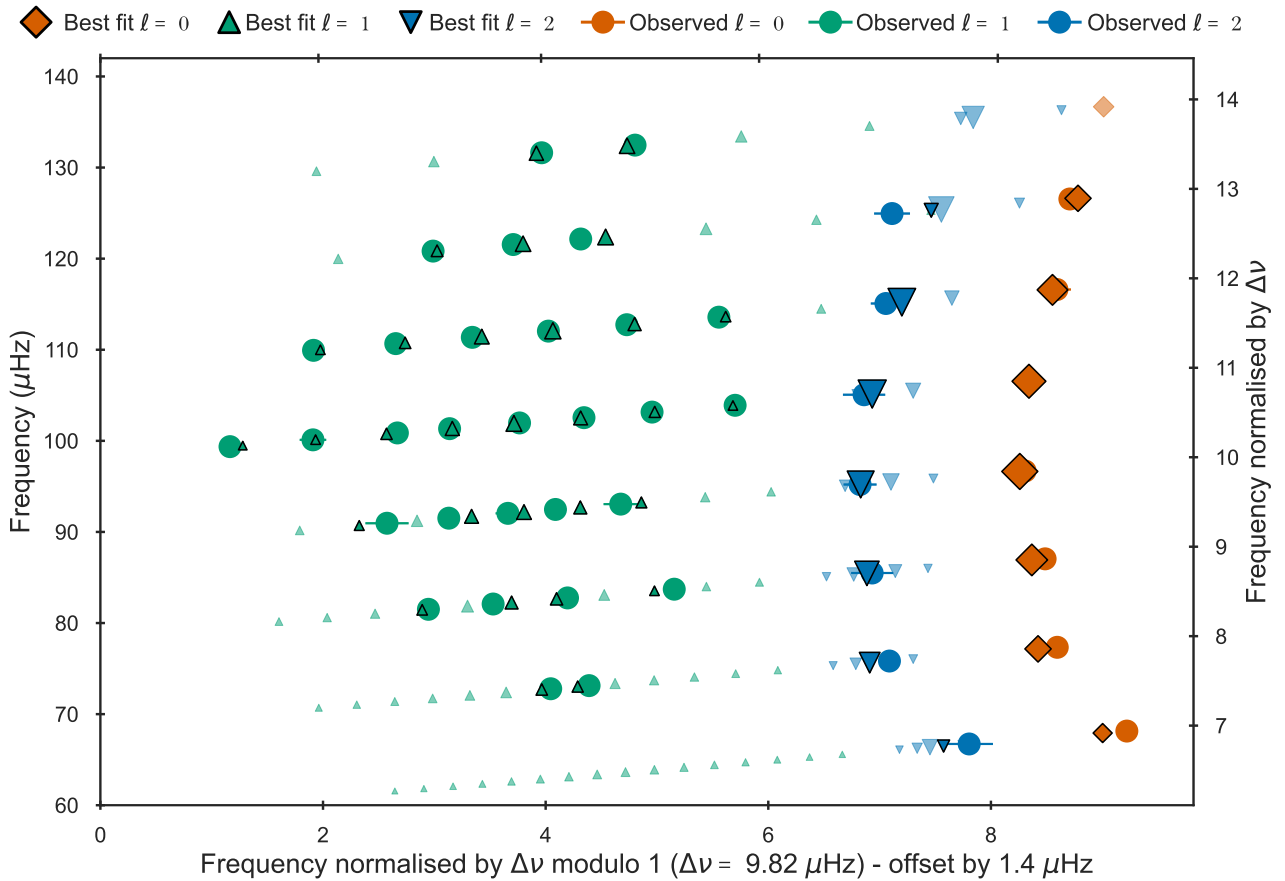


**Fig. 6.** Échelle diagram of Hennes with the fitted individual frequencies matched to the modes of the best-fitting model. The orange diamonds, green upwards and blue downwards triangles depict the  $\ell = 0$ ,  $\ell = 1$  and  $\ell = 2$  modes, respectively. The cubic term of the surface correction by Ball & Gizon (2014) has been applied to the model frequencies, with a surface correction coefficient of  $a_3 = -3.9976 \cdot 10^{-8}$ . The size of the model modes is scaled related to the inverse of their respective inertia.

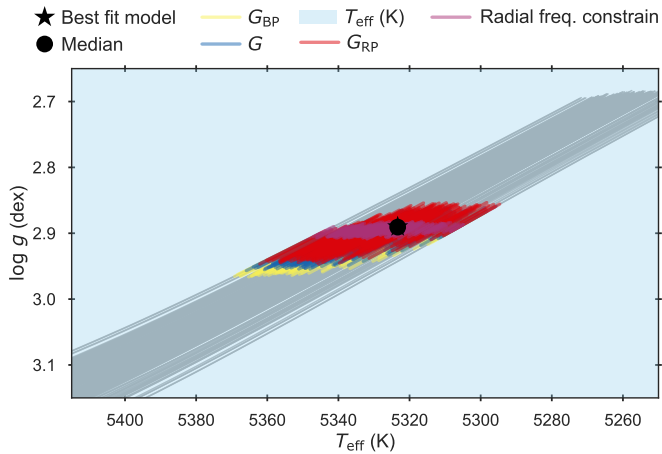


**Fig. 7.** Kiel diagram of Hennes displaying a representative number of stellar tracks in the grid. The observed constraints on the fitted parameters are overlaid to show an overlap with the median and best-fitting model from the posterior.

model, e.g. see the three lowest radial modes in the figure that deviate due to significant curvature of the observed ridge (Mosser et al. 2013). Hence a difference of  $\sim 1.5\sigma$  is to be expected, however this difference is reduced when comparing to alternative estimates of the observed  $\Delta\nu$  by some independent determi-

**Table 4.** Modelling results for Hennes. All stellar parameters are given by the median of the posterior distribution from BASTA, with uncertainties as the 16th and 84th quantiles.

Hennes – KIC 4671239			
Stellar parameter	This work	A16	Alencastro Puls et al. 2022
$M [M_{\odot}]$	$0.79^{+0.04}_{-0.03}$	$1.00^{+0.10}_{-0.08}$	$1.01^{+0.02}_{-0.02}$
$R [R_{\odot}]$	$5.29^{+0.08}_{-0.07}$	$5.73^{+0.19}_{-0.17}$	$5.70^{+0.05}_{-0.05}$
Age [Gyr]	$12.3^{+1.7}_{-1.7}$	$5.28^{+1.90}_{-1.48}$	$5.4^{+0.4}_{-0.3}$
$\nu_{\max} [\mu\text{Hz}]$	$91.34^{+0.87}_{-0.83}$	–	–
$\Delta\nu [\mu\text{Hz}]$	$9.74^{+0.02}_{-0.01}$	–	–
$\Delta\Pi_1 [\text{s}]$	$67.32^{+0.58}_{-0.51}$	–	–

nations (see Table A.1). Notably, the predicted  $\nu_{\max}$  value from the fit deviates significantly from the observed. This discrepancy is discussed in detail in Sect. 6.2.

Figure 7 illustrates the result in a Kiel diagram (a spectroscopic HR diagram) plotting the surface gravity  $\log(g)$  against effective temperature. Only the tracks containing statistically significant models are plotted, forming the dense distribution of stellar tracks seen. The observational constraints for the fitted parameters are overlaid onto the plot for a representative region along each track depicting the  $1\text{-}\sigma$  uncertainty (Hjørringgaard et al. 2017). Notably, the frequency constraint band is formed based on a selection of models matching the radial fre-

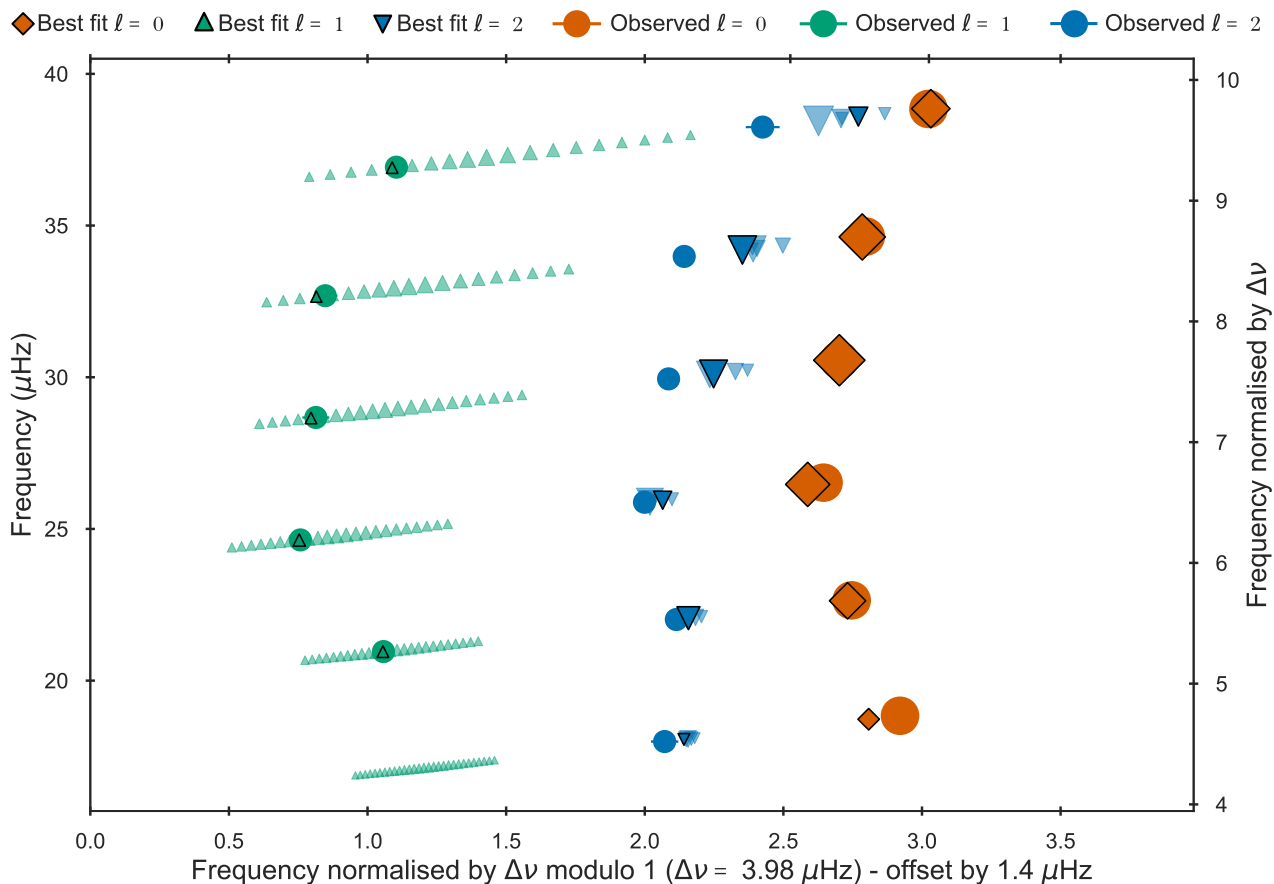


**Fig. 8.** Échelle diagram of Rogue with the fitted individual frequencies matched to the modes of the best-fitting model. The orange diamonds, green upwards and blue downwards triangles depict the  $\ell = 0$ ,  $\ell = 1$  and  $\ell = 2$  modes, respectively. The cubic term of the surface correction by Ball & Gizon (2014) has been applied to the model modes, with a surface correction coefficient of  $a_3 = -1.5554 \cdot 10^{-7}$ . The size of the model modes is scaled related to the inverse of their respective inertia.

quencies, not taking into account the non-radial oscillations in the spectrum. The results display a satisfactory overlap between all observational constraints. Importantly, this kind of overlap remained unattainable for A16 when fitting the global asteroseismic parameters. Crucially, this inconsistency persists in this work if we fit the global asteroseismic parameters (see Appendix C). Hence, a proper inference for Hennes is only attainable when utilising the individual mode frequencies to avoid the dependence on the asteroseismic scaling relations, as has been presented here.

### 5.2. Rogue – KIC7693833

The results obtained for Rogue are displayed in Table 5, where the prior results of A16 are also included. For inspection of the posteriors, see Fig. B.2. The obtained parameters in this work indicate a low-mass star with an accordingly high age. These results are in tension with the initial estimates by A16, yet now comply with the expectations for a low-metallicity star.

Figure 8 displays the fit to the individual frequencies for Rogue. The more evolved nature of the best-fitting model is immediately apparent from the denser theoretical frequency spacing for each acoustic mode order. The fit to the individual frequencies is satisfying, however with some artefacts of the frequency matching algorithm impacting the quadrupole modes. This will be further discussed in Sect. 6.1. The modelled  $\Delta\nu$  value is slightly higher than the observed. This is due to the  $\Delta\nu$

**Table 5.** Modelling results for Rogue. All stellar parameters are given by the median of the posterior distribution from BASTA, with uncertainties as the 16th and 84th quantiles.

Rogue – KIC 7693833		
Stellar parameter	This work	A16
$M [M_{\odot}]$	$0.83^{+0.03}_{-0.01}$	$0.97^{+0.12}_{-0.10}$
$R [R_{\odot}]$	$9.53^{+0.14}_{-0.06}$	$10.03^{+0.48}_{-0.42}$
Age [Gyr]	$10.3^{+0.6}_{-1.4}$	$6.29^{+3.19}_{-2.20}$
$\nu_{\max} [\mu\text{Hz}]$	$29.83^{+0.27}_{-0.23}$	–
$\Delta\nu [\mu\text{Hz}]$	$4.072^{+0.01}_{-0.004}$	–
$\Delta\Pi_1 [s]$	$53.62^{+0.32}_{-0.99}$	–

value in the grid being estimated from a weighted average between the non-surface-corrected radial frequencies. Hence, the obtained value will be somewhat higher, but by inspection of Fig. 8 is suitable for creating the vertical ridge structure in the échelle diagram. It may be noted that the modelled period spacing of  $\Delta\Pi_1 = 53.6^{+0.3}_{-1.0}$  s is roughly in accordance with the uncertain observational estimate of  $\Delta\Pi_1 = 56.6$  s discussed in Sect. 3.2. The  $\nu_{\max}$  discrepancy found for Hennes is also clear for Rogue.

Figure 9 illustrates the result in a Kiel diagram, similar to that made for Hennes. At first glance, it appears counter-intuitive

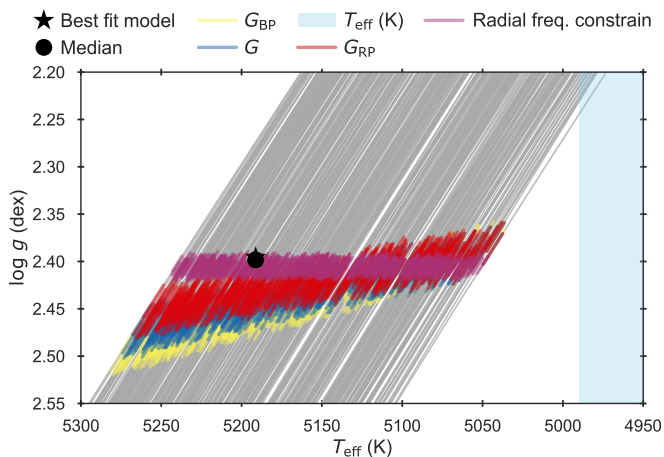


**Fig. 9.** Kiel diagram of Rogue displaying a representative number of stellar tracks in the grid. The observed constraints on the fitted parameters are overlaid to show an overlap with the median and best-fitting model from the posterior. A clear discrepancy between the observed and modelled temperature is found, with the lower  $1-\sigma$  uncertainty visualised by the boundary of the blue region.

why the best-fitting model and median posterior solutions do not lie at lower temperatures where the frequency constraints overlap perfectly with the Gaia magnitudes. This is because the frequency constraint band is formed based on the radial frequencies only, allowing the best-fitting model and median solutions, which take into account the complete mode spectrum and other fit parameters, to lie away from the visual overlap. A clear  $\sim 2.3\sigma$  deviation from the observed temperature is found, an unresolved complication present for Rogue. Crucially, the best-fitting model and seismic solution is consistent with all other observables, and provide a modelling result, which is not in tension with prior expectations from the low-metallicity nature of the star. In Sect. 6.1 we discuss the nuances of the modelling challenges for Rogue, where a more thorough evaluation will be presented.

## 6. Asteroseismic characterisation from individual frequency modelling

This work has demonstrated that rigorous asteroseismic modelling is feasible for evolved red giants, even in the most challenging cases of the very low-metallicity regime. We emphasize that the results obtained are not reproduced if one considers the global asteroseismic parameters in the fitting (see Appendix C). This suggests that future studies of red giants could benefit from relying more on the individual frequencies as direct observable constraints in the modelling.

Hennes is the first star with  $\nu_{\max}$  below  $100\ \mu\text{Hz}$  to be asteroseismically modelled with mixed-mode individual frequencies within a grid-based methodology. Importantly, at this stage of evolution, we can clearly observe several dipole mixed modes within each acoustic mode order. As shown in Fig. 6, this allows us to capture the underlying period spacing during the modelling, effectively providing constraints on the interior stellar structure. Rogue further extends the coverage of stars with asteroseismic individual frequency modelling to the region where  $\nu_{\max}$  is below  $35\ \mu\text{Hz}$ . Here, the mixed mode pattern has become so dense and the period spacing so low that we cannot confidently resolve the dipole mixed modes observationally. Addi-

tionally, the inertia of the g-dominated modes increases, making their detection difficult. Only the observational estimate for the acoustic resonances of each mode order were fitted; however to models containing all potentially observable mixed modes, which allows for the opportunity of matching several theoretical frequencies. This allowed for the classification of a particularly vexing star; however, a significant temperature discrepancy between the observed and modelled values persists.

### 6.1. Modelling nuances of Rogue

In Fig. 9 a clear discrepancy between the observed and modelled temperature was seen. A likely cause was mentioned in Sect. 2.1, namely the application of 1D NLTE spectroscopic reduction methods for the very low-metallicity regime. The degeneracy between the temperature and metallicity, as well as the implementation of the microturbulence as a fitting parameter, may very well lead to inconsistencies on the observational side. Furthermore, the temperature of the RGB stellar models is also a topic of discussion. Cassisi (2017) showed how the temperature of RGB models is sensitive to  $\alpha_{\text{MLT}}$  and the outer boundary condition employed in the  $T(\tau)$  relation for the choice of atmosphere. These aspects were further outlined by Tayar et al. (2017), who presented a metallicity dependent temperature offset for RGB stars when compared to theoretical predictions, suggesting to make the convective mixing length metallicity dependent to account for the effect. Salaris et al. (2018) later reanalysed the sample from Tayar et al. (2017), and found that the discrepancy was only significant for  $\alpha$ -enhanced RGB stars. Schonhut-Stasik et al. (2024) also argued that the choice of temperature scales for low-metallicity red-giant models may lead to discrepancies. It is noteworthy that this temperature discrepancy was not present for Hennes while being so prominent for Rogue. A planned future study employing a larger sample of low-metallicity giants will likely aid in classifying the occurrence and behavioural trends of the temperature discrepancy.

In the frequency fit of Rogue in Fig. 8, certain quadrupole modes appear to be mismatched, for example in the highest mode order. The frequency matching algorithm in BASTA was developed for main-sequence and sub-giant stars (see e.g. Stokholm et al. 2019). For the former, only one mode exists per acoustic mode order and for the latter there is a large difference in mode inertia between the few modes in each mode order. On the RGB and with the oscillation spectra obtained through the application of the truncated scanning method of Larsen et al. (2024), we obtain a modest number of mixed modes closely spaced in frequency and of comparable inertia within each mode order. This means that the matching algorithm described briefly in Sect. 4.2.1 may not be entirely suitable for application to red giants. However, we stress that forcing the solution to the "by-eye" optimal solution for the best-fitting model in Fig. 8 has no impact on the choice of optimal model during the fitting. A test was carried out simply matching the observed mode of each degree to the respective model frequency with the lowest inertia within each acoustic mode order. This does not significantly change the drawn posteriors, as the contribution to the likelihood from the above change is less significant than the evolution of particularly the radial frequency spectrum between consecutive models. A proper evaluation of a refined RGB mixed-mode frequency matching algorithm requires statistics on the performance based on more than the two stars at hand, which is the subject of a future study.

## 6.2. Circumventing the $\nu_{\max}$ scaling relation dependence

The estimates for  $\nu_{\max}$  obtained from the modelling posteriors showed a significant discrepancy to the observed for both stars. To reiterate, the  $\nu_{\max}$  value of the models are predicted using the scaling relation in Eq. 2 as no other alternative exists. We circumvented the dependence on the scaling relations entirely by fitting the individual frequencies, resulting in the highest-likelihood models being selected based on the direct constraints that the frequencies provide to the interior model structures. This difference suggests a metallicity dependence on the  $\nu_{\max}$  scaling relation, which becomes significant for very low-metallicity stars. This agrees with the dependence of  $\nu_{\max}$  to the Mach number found by Belkacem et al. (2011).

Investigating this metallicity dependence means evaluating a correction factor to the scaling relation,

$$\nu_{\max} = f_{\nu_{\max}} \nu_{\max, \text{scal}} \simeq f_{\nu_{\max}} \left( \frac{M}{M_{\odot}} \right) \left( \frac{R}{R_{\odot}} \right)^{-2} \left( \frac{T_{\text{eff}}}{T_{\text{eff}, \odot}} \right)^{-1/2} \nu_{\max, \odot},$$

$$f_{\nu_{\max}} = \frac{\nu_{\max, \text{obs}}}{\nu_{\max, \text{BFM}}}.$$

Here,  $\nu_{\max, \text{BFM}}$  can be extracted from the best-fitting model of Hennes and Rogue while  $\nu_{\max, \text{obs}}$  are the observed values shown in Table 2. The values are  $\nu_{\max, \text{BFM}} = 91.26$  and  $\nu_{\max, \text{BFM}} = 29.60 \mu\text{Hz}$ , resulting in correction factors of  $f_{\nu_{\max}} = 1.084$  and  $f_{\nu_{\max}} = 1.098$ , for Hennes and Rogue, respectively. This yields a difference in  $\nu_{\max}$  of 8 – 10%, showing that the  $\nu_{\max}$  scaling relation in the metal-poor regime is significantly less accurate than near solar metallicities. We can express this difference in mass using the observed  $\nu_{\max}$ ,  $\Delta\nu$  and  $T_{\text{eff}}$  to calculate the scaling relation estimate as,

$$M = \left( \frac{\nu_{\max, \text{obs}}}{\nu_{\max, \odot}} \right)^3 \left( \frac{\Delta\nu}{\Delta\nu_{\odot}} \right)^{-4} \left( \frac{T_{\text{eff}}}{T_{\text{eff}, \odot}} \right)^{-1/2}, \quad (3)$$

$$= f_{\nu_{\max}}^3 \left( \frac{\nu_{\max, \text{BFM}}}{\nu_{\max, \odot}} \right)^3 \left( \frac{\Delta\nu}{\Delta\nu_{\odot}} \right)^{-4} \left( \frac{T_{\text{eff}}}{T_{\text{eff}, \odot}} \right)^{-1/2}. \quad (4)$$

Using the scaling relation in Eq. 3, this results in a  $\sim 30\%$  and  $\sim 46\%$  larger mass from the scaling relation than from the determination when performing asteroseismic individual frequency modelling. This seconds the findings of Huber et al. (2024) who similarly recovered a  $\sim 24\%$  difference in mass for KIC 8144907 with  $[\text{Fe}/\text{H}] = -2.66$  dex. The tension remains when using proposed  $\Delta\nu$  metallicity corrections (Viani et al. 2017) and repeating the above exercise. For these three RGB stars with individual frequency modelling, the situation thus hints towards an increasing discrepancy with evolution for these similarly very metal-poor giants.

Lastly, we note that for the stars KIC 7341231 (Deheuvels et al. 2012),  $\nu$  Indi (Chaplin et al. 2020) and HD 140283 (Lundkvist et al. in prep) with individual frequency modelling shown overplotted in Fig. 1, the tentative metallicity dependence on  $\nu_{\max}$  between observed and model values was also seen.

## 6.3. Enhanced mode mixing at low metallicity

During this work concerning stellar modelling of low-metallicity giants, a property of the interior profiles in the models was noticed. The extent of the evanescent region was increased and the coupling weakened with increasing metallicity. Here, we wish to briefly clarify and present this trend seen in the models.

Figure 10 depicts a propagation diagram of three stellar models, showing the proximity of the oscillation cavities in the

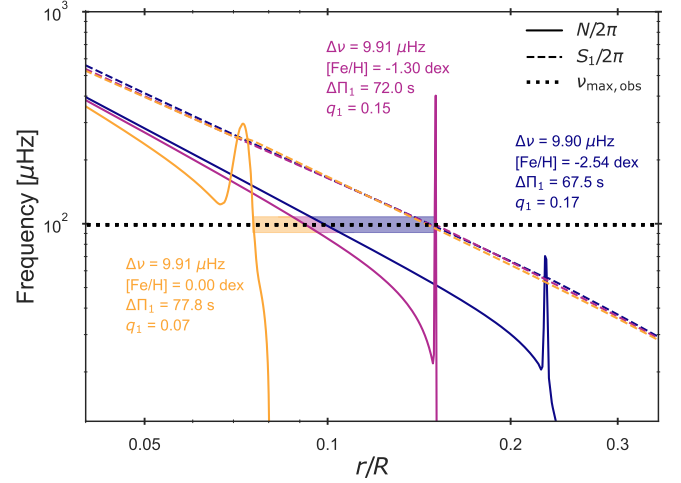


**Fig. 10.** Propagation diagram for three stellar models depicting the characteristic frequencies in the interior near the lower convective boundary. The best-fitting model of Hennes is plotted alongside two models of similar evolutionary state, i.e. similar  $\Delta\nu$  value, with identical initial parameters but a variation in  $[\text{Fe}/\text{H}]$ . The shaded region around the observed  $\nu_{\max}$  of Hennes represents the extent of the evanescent region for the three models, which increases with metallicity.

deep interior of the models. The very low-metallicity model is the best-fitting model of Hennes. The other two were calculated with identical initial parameters and varying the metallicity to  $[\text{Fe}/\text{H}] = -1.3$  and  $[\text{Fe}/\text{H}] = 0.0$ . The buoyancy frequency  $N$  (Tassoul 1980) and Lamb frequency  $S_{\ell}$  (Lamb 1932) are calculated using Eqs. 2 and 3 of Larsen et al. (2024), respectively. The figure indicates that the depth of the convective zone deepens with increasing metallicity, in coherence with convection being known to have a dependence on the opacity and thus chemical composition. This effectively increases the extent of the evanescent region (as shown by the shaded bands of each model) for a representative frequency here chosen as the observed  $\nu_{\max}$  of Hennes. Equations 11 and 12 of Hekker & Christensen-Dalsgaard (2017) allows us to evaluate the dipole period spacing and Eq. 9 of Larsen et al. (2024) provides an estimate of the coupling constant. The obtained values, overplotted on Fig. 10, clearly illustrate the same trend: a decreasing period spacing and increasing coupling constant with decreasing metallicity.

This effect should lead to a stronger mixing between the p- and g-modes of low-metallicity stars, resulting in a larger frequency displacement for the mixed modes within a given acoustic order. Additionally, the difference in the period spacing and coupling constant will affect Eq. 28 of Mosser et al. (2018), which describes the frequency range in which mixed modes should be observable around an acoustic resonance, hinting towards a possible metallicity dependence. Confirming the postulated property of mixed-mode behaviour as a function of metallicity would require a dedicated study of the trend in observed oscillation spectra of RGB stars, which is beyond the scope of this work.

## 6.4. Galactic context

The Galactic orbital characteristics of the stars were determined from the 5D astrometric information and line-of-sight velocities from *Gaia* DR3 (Gaia Collaboration et al. 2016,

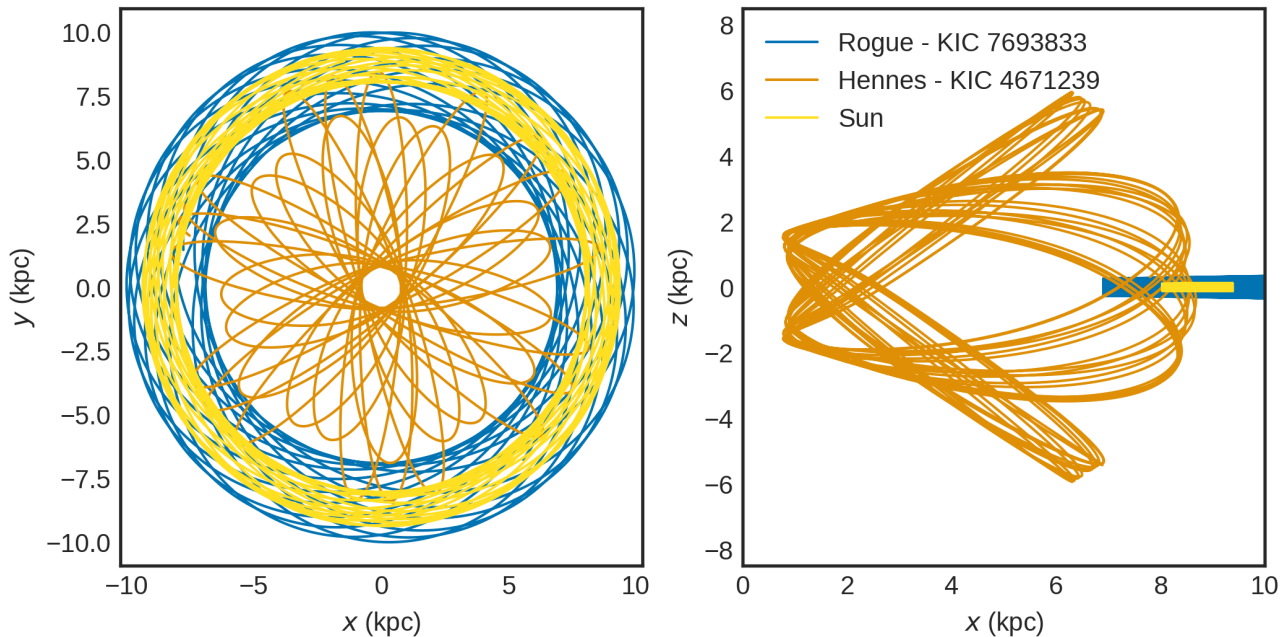


**Fig. 11.** The integrated orbit of Rogue and Hennes within the Milky Way’s potential over a 10 Gyr period, depicted in Cartesian Galactocentric coordinates. The left panel presents a top-down view of the Galaxy ( $x, y$ ), while the right panel shows an edge-on perspective ( $x, z$ ). The Sun’s integrated orbit is included in both views as a reference.

2023). We use the PYTHON package `galpy` (Bovy 2015) for this computation of the Galactic orbital properties. As a description of the Milky Way potential, we use the axisymmetric gravitational potential `McMillan2017` (McMillan 2017). As for the Galactic location and velocity of the Sun, we assume  $(X_{\odot}, Y_{\odot}, Z_{\odot}) = (8.2, 0, 0.0208)$  kpc and  $(U_{\odot}, V_{\odot}, W_{\odot}) = (11.1, 12.24, 7.25)$  km s $^{-1}$  with a circular velocity of 240 km s $^{-1}$  (Schönrich et al. 2010; Bennett & Bovy 2019; Gravity Collaboration et al. 2019).

We use the implementation of the action-angle estimation algorithm *Stäckel fudge* (Binney 2012) in `galpy` with a focal length focus of 0.45 to calculate orbit information such as actions, eccentricity, and maximum orbit Galactocentric height. By leveraging the uncertainties and correlations in the astrometric measurements to create a multivariate normal distribution, we perform 10,000 iterations to generate distributions of the orbital properties. The 16th, 50th, and 84th percentiles of these distributions are then used as numerical estimates of the orbital values and their associated uncertainties. The complete list of orbital properties for Hennes and Rogue can be found in Table D.1 in the Appendix.

Fig. 11 illustrates the integrated orbits of Hennes and Rogue within the Milky Way’s gravitational potential, highlighting their differing extents. Hennes traverses the dense inner regions of the Galaxy, with an inner turning point nearly 1 kpc from the Galactic centre. Additionally, Hennes frequently moves far from the Galactic disk, reaching heights several kiloparsecs above the Galactic midplane. In contrast, while Rogue does venture beyond the Local Solar Neighbourhood, its orbit more closely resembles that of the Sun, differing significantly from the more extensive and dynamic path of Hennes.

Fig. 12 shows the location of the stars in a Toomre diagram, in which the horizontal axis depicts motion around in the plane and the vertical axis represents motion perpendicular to the horizontal axis. This representation helps distinguish different Galactic components more clearly. In this context, Hennes stands out as behaving like a typical halo star, characterized by

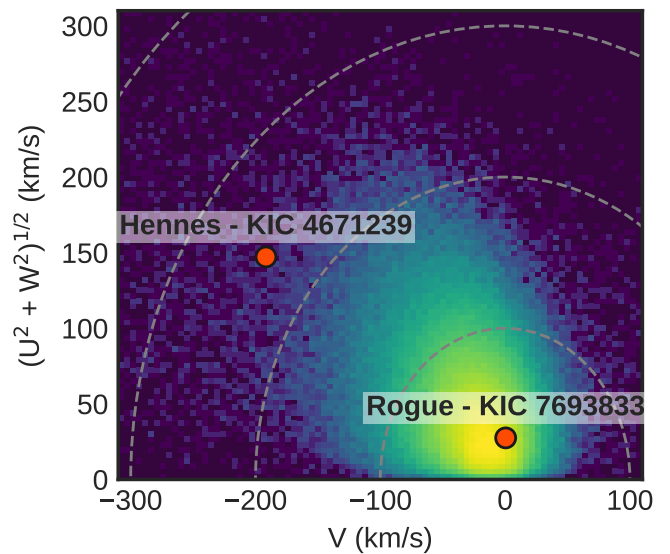


**Fig. 12.** A Toomre diagram showing the Galactic velocity components, with the vertical axis representing motion perpendicular to the plane and the horizontal axis depicting motion within the plane. The location of Hennes and Rogue in this space are marked with red dots. The background density map represents the number count of single targets from *Gaia* DR3 with reliable astrometric data and available line-of-sight velocities (astrometric\_params\_solved = 95, non\_single\_star = 0, ruwe < 1.4, and rv\_nb\_transits > 0).

its lower rotational velocity within the Galactic plane and higher velocities in the vertical (up-down) and radial (in-out) directions compared to the Sun. Rogue is more intriguing, as it appears to align with the characteristics of a thin disk star, exhibiting only slightly higher velocities in the direction perpendicular to the Galactic plane.

### 6.4.1. Possible Galactic origins

In this section, we assess the possible Galactic origins of the two stars based on their combined kinematics, spectroscopic, and age signatures.

Kinematically Hennes looks like a characteristic halo star. It has a low orbital energy and the orbit looks kinematically heated in velocities, eccentricity, and angular momentum. The position of Hennes in angular momenta-orbital energy dimensions could place it in either L-RL3 (Ruiz-Lara et al. 2022; Dodd et al. 2023), Heracles (Horta et al. 2021), or in a metal-poor tail of Gaia-Enceladus (Helmi et al. 2018). In either of these cases, Hennes would be the most metal-poor member of each association discovered to date.

The orbit of Rogue is similar to those of the older members of the Galactic thin disk, which is peculiar given its age and metallicity. This suggests that Rogue is part of this controversial, ancient and very metal-poor stellar population in the Milky Way. The discovery of very metal-poor stars exhibiting disc-like kinematics and a preference for prograde over retrograde orbits has recently generated significant interest within the community (Sestito et al. 2019; Cordoni et al. 2021; Belokurov & Kravtsov 2022; Carollo et al. 2023; Bellazzini et al. 2024; Arden-Arentsen et al. 2024; Fernández-Alvar et al. 2024). Studies of these metal-poor stars with prograde planar orbits can provide us insights into the earliest phase of the formation of the Milky Way discs and there is still many unanswered questions. From simulations of model galaxies, Sotillo-Ramos et al. (2023) found that the fraction of very metal-poor stars in the kinematically cold disc component varies from 5 – 10 % up to 40 %, with typical values around 20 % and an occurrence rate that seem to decrease with decreasing metallicity. Other comparisons with simulations of Milky Way analogues suggests that most stars in this population likely originated from accretion events on nearly planar orbits (Sestito et al. 2021) as the emergence of this population is unlikely to be induced by a rotating galactic bar (Yuan et al. 2024). Nepal et al. (2024) emphasized that many disc galaxies at high redshifts possess an ancient and kinematically cold disc formed in situ, suggesting that this metal-poor population could represent our Galaxy’s analogue.

If Rogue is representative of the population, then we can use its stellar age as a constraint when assessing the possible origins. Rogue is more aligned with the view that this population originates from multiple accretion events in which the accretion occurred close to planar orbits. Rogue could also originate from being in a thick disk or halo population that has transitioned into an orbits closer to the Galactic midplane. The age of Rogue is in tension with the view that an ancient metal-poor thin disc as this disc should have formed  $> 13$  Gyr ago which is significantly prior to the formation of Rogue. As it is possible that multiple channels contribute to the formation of this population, with Rogue belonging to one and not the other, a future study employing asteroseismology for this population of stars appears to be the next step.

## 7. Conclusion

This work proves that asteroseismic individual frequency modelling is possible within the grid-based modelling scheme for evolved red giants. Proper determination of global stellar properties in the very metal-poor regime has been shown to crucially depend on how the stellar inference is made. The main conclusions of this paper are as follows:

- The two very low-metallicity stars, KIC 4671239 and KIC 7693833, have been characterised with stellar properties that are coherent with expectations from Galactic archaeology. Hennes and Rogue were found to have masses of  $0.79^{+0.04}_{-0.03}$  and  $0.83^{+0.03}_{-0.01} M_{\odot}$  with an age of  $12.3^{+1.7}_{-1.7}$  and  $10.3^{+0.6}_{-1.4}$  Gyr, respectively. Both stars had for a long time defied such characterisation, as they are situated in a very difficult region of parameter space for stellar modelling, yet individual frequency modelling in combination with detailed grid-based approaches has made it possible. Crucially, the obtained self-consistency could not be obtained when fitting the global asteroseismic parameters in the past nor in the contemporary work. This fact speaks to the benefits of future application of individual frequency modelling for giants.
- A metallicity dependence of the asteroseismic scaling relation for  $\nu_{\max}$  was seen through a clear discrepancy between the observed and modelled values for Hennes and Rogue of  $\sim 8\text{--}10\%$ , with the  $\nu_{\max}$  predicted from the asteroseismic scaling relation being too small compared to the observations. In the determination of global stellar properties for very metal-poor stars in general, such a difference would correspond to overestimations in mass by  $\sim 30\%$ , leading to wrongful conclusions about the age demographics of the population. This result is in coherence with prior findings by Belkacem et al. (2011) and Huber et al. (2024). Yet, it is also in slight tension with studies by Zhou et al. (2024), finding that for the case of main sequence stars  $\nu_{\max}$  shows no metallicity dependence. However, the conclusion of Zhou et al. (2024) may not hold in the case of more evolved stars in the sub-giant or red-giant branch phases of their lives. To answer this question definitively will require further studies on both the theoretical and observational side, something which is currently in progress.
- Accurate and precise stellar ages are crucial for unravelling the timeline of events in the Galaxy. The impact of the systematic effect of metallicity on the  $\nu_{\max}$  scaling relation can be significant for Galactic archaeology as asteroseismic targets are typically used as calibrators. In recent years, stellar remnants of galaxies that merged with the early Milky Way have been a particular topic of interest for the community (see e.g. Helmi 2020, for a review). We have identified Hennes to be a member of one of such halo populations, making it the most metal-poor member with detailed modelling using asteroseismic constraints. Rogue seems to be a member of the ancient very metal-poor population with prograde, planar orbits; providing a valuable age constraint to studies of the earliest phase of the formation of the Milky Way disc structures.

We emphasise the possibilities of circumventing the dependence on the asteroseismic scaling relations and directly fitting the individual frequencies of red giants. Observationally, *Kepler* and the work by observational astronomers has supplied us with high-quality detection of the individual frequencies of giants, which is continuously being expanded by missions such as the Transiting Exoplanet Survey Satellite (TESS; Ricker et al. 2014) and in the future the PLANetary Transits and Oscillations of stars mission (PLATO; Rauer et al. 2024). It is now possible following the work by Larsen et al. (2024) to utilise the individual frequencies to their full potential and this paper has demonstrated that it works in one of the most challenging regions for stellar modelling. We therefore suggest that such efforts should be pursued in the future as it may allow for refinement of our understanding of stars on the RGB. For example, investigations resolving the

convective zone boundaries probed by the period spacing  $\Delta\Pi_1$  could be further developed by the inclusion of the mixed-mode dipole individual frequencies, which directly probes this region in the stellar interior through their sensitivity to the mode coupling (Jiang & Christensen-Dalsgaard 2014; Pinçon et al. 2019). These efforts in turn link to the study of the origin behind magnetic fields in red giant stars (see e.g., Deheuvels et al. 2023; Bharati Das et al. 2024); a field of research still in its infancy.

*Acknowledgements.* JRL wishes to thank the members of SAC for comments and discussions regarding the paper. Furthermore, we appreciate being given access to the data for and the allowed inclusion of Fig. 1 by Dan Huber.

This work was supported by a research grant (42101) from VILLUM FONDEN. Funding for the Stellar Astrophysics Centre was provided by The Danish National Research Foundation (grant agreement no.: DNRFF106). MSL acknowledges support from The Independent Research Fund Denmark's Inge Lehmann program (grant agreement no.: 1131-00014B). The numerical results presented in this work were obtained at the Centre for Scientific Computing, Aarhus <https://phys.au.dk/forskning/faciliteter/cscaa/>. AS acknowledges support from the European Research Council Consolidator Grant funding scheme (project ASTEROCHRONOMETRY, G.A. n. 772293, <http://www.asterochronometry.eu>).

This work presents results from the European Space Agency (ESA) space mission Gaia. Gaia data are being processed by the Gaia Data Processing and Analysis Consortium (DPAC). Funding for the DPAC is provided by national institutions, in particular the institutions participating in the Gaia MultiLateral Agreement (MLA). The Gaia mission website is <https://www.cosmos.esa.int/gaia>. The Gaia archive website is <https://archives.esac.esa.int/gaia>. This paper includes data collected by the Kepler mission and obtained from the MAST data archive at the Space Telescope Science Institute (STScI). Funding for the Kepler mission is provided by the NASA Science Mission Directorate. STScI is operated by the Association of Universities for Research in Astronomy, Inc., under NASA contract NAS 5–26555.

SH acknowledges support from the European Research Council under the European Community's Horizon 2020 Framework/ERC grant agreement no 101000296 (DipolarSounds).

## Data availability

All data and stellar grid products are available upon reasonable request to the first author.

## References

Abdurro'uf, Accetta, K., Aerts, C., et al. 2022, *ApJS*, 259, 35  
 Aguirre Børsen-Koch, V., Rørsted, J. L., Justesen, A. B., et al. 2022, *MNRAS*, 509, 4344  
 Alencastro Puls, A., Casagrande, L., Monty, S., et al. 2022, *MNRAS*, 510, 1733  
 Anderson, E. R., Duvall, Thomas L., J., & Jefferies, S. M. 1990, *ApJ*, 364, 699  
 Angulo, C., Arnould, M., Rayet, M., et al. 1999, *Nucl. Phys. A*, 656, 3  
 Antonov, I. & Saleev, V. 1980, *USSR Computational Mathematics and Mathematical Physics*, 19, 252  
 Appourchaux, T., Antia, H. M., Benomar, O., et al. 2014, *A&A*, 566, A20  
 Ardern-Arentsen, A., Monari, G., Queiroz, A. B. A., et al. 2024, *MNRAS*, 530, 3391  
 Asplund, M., Grevesse, N., Sauval, A. J., & Scott, P. 2009, *ARA&A*, 47, 481  
 Ball, W. H. & Gizon, L. 2014, *A&A*, 568, A123  
 Ball, W. H., Themeßl, N., & Hekker, S. 2018, *MNRAS*, 478, 4697  
 Balsev, D. S. 2006, *AJ*, 132, 2326  
 Basu, S. & Chaplin, W. J. 2017, *Asteroseismic Data Analysis: Foundations and Techniques*  
 Bedding, T. R. 2014, in *Asteroseismology*, ed. P. L. Pallé & C. Esteban, 60  
 Bedding, T. R., Huber, D., Stello, D., et al. 2010, *ApJ*, 713, L176  
 Bedding, T. R., Mosser, B., Huber, D., et al. 2011, *Nature*, 471, 608  
 Belkacem, K., Goupil, M. J., Dupret, M. A., et al. 2011, *A&A*, 530, A142  
 Bellazzini, M., Massari, D., Ceccarelli, E., et al. 2024, *A&A*, 683, A136  
 Belokurov, V. & Kravtsov, A. 2022, *MNRAS*, 514, 689  
 Bennett, M. & Bovy, J. 2019, *MNRAS*, 482, 1417  
 Benomar, O., Appourchaux, T., & Baudin, F. 2009, *A&A*, 506, 15  
 Benomar, O., Bedding, T. R., Mosser, B., et al. 2013, *ApJ*, 767, 158  
 Bergemann, M., Lind, K., Collet, R., Magic, Z., & Asplund, M. 2012, *MNRAS*, 427, 27  
 Bharati Das, S., Einramhof, L., & Bugnet, L. 2024, *arXiv e-prints*, [arXiv:2405.20133](https://arxiv.org/abs/2405.20133)

Binney, J. 2012, *MNRAS*, 426, 1324  
 Borre, C. C., Aguirre Børsen-Koch, V., Helmi, A., et al. 2022, *MNRAS*, 514, 2527  
 Borucki, W. J., Koch, D., Basri, G., et al. 2010, *Science*, 327, 977  
 Bovy, J. 2015, *ApJS*, 216, 29  
 Bratley, P. & Fox, B. 1988, *ACM Transactions on Mathematical Software*, 14, 88  
 Brogaard, K., VandenBerg, D. A., Bruntt, H., et al. 2012, *A&A*, 543, A106  
 Brown, T. M., Gilliland, R. L., Noyes, R. W., & Ramsey, L. W. 1991, *ApJ*, 368, 599  
 Carollo, D., Christlieb, N., Tissera, P. B., & Sillero, E. 2023, *ApJ*, 946, 99  
 Casagrande, L., Silva Aguirre, V., Stello, D., et al. 2014, *ApJ*, 787, 110  
 Cassisi, S. 2017, in *European Physical Journal Web of Conferences*, Vol. 160, European Physical Journal Web of Conferences, 04002  
 Castelli, F. & Kurucz, R. L. 2004, *ArXiv Astrophys. e-prints [arXiv:0405087]*  
 Chaplin, W. J. & Miglio, A. 2013, *ARA&A*, 51, 353  
 Chaplin, W. J., Serenelli, A. M., Miglio, A., et al. 2020, *Nature Astronomy*, 4, 382  
 Christensen-Dalsgaard, J. 2008, *Ap&SS*, 316, 113  
 Cooke, R. J. & Fumagalli, M. 2018, *Nature Astronomy*, 2, 957  
 Cordoni, G., Da Costa, G. S., Yong, D., et al. 2021, *MNRAS*, 503, 2539  
 Corsaro, E. 2019, *Frontiers in Astronomy and Space Sciences*, 6, 21  
 Corsaro, E. & De Ridder, J. 2014, *A&A*, 571, A71  
 Corsaro, E., Mathur, S., García, R. A., et al. 2017, *A&A*, 605, A3  
 Corsaro, E., McKeever, J. M., & Kuszlewicz, J. S. 2020, *A&A*, 640, A130  
 Cunha, M. S., Damasceno, Y. C., Amaral, J., et al. 2012, *ApJ*, 756, 19  
 Cunha, M. S., Stello, D., Avelino, P. P., Christensen-Dalsgaard, J., & Townsend, R. H. D. 2015, *ApJ*, 805, 127  
 Däppen, W., Mihalas, D., Hummer, D. G., & Mihalas, B. W. 1988, *ApJ*, 332, 261  
 Davies, G. R., Handberg, R., Miglio, A., et al. 2014, *MNRAS*, 445, L94  
 Davies, G. R., Silva Aguirre, V., Bedding, T. R., et al. 2016, *MNRAS*, 456, 2183  
 Deheuvels, S., Ballot, J., Gehan, C., & Mosser, B. 2022, *A&A*, 659, A106  
 Deheuvels, S., García, R. A., Chaplin, W. J., et al. 2012, *ApJ*, 756, 19  
 Deheuvels, S., Li, G., Ballot, J., & Lignières, F. 2023, *A&A*, 670, L16  
 Dhanpal, S., Benomar, O., Hanasoge, S., et al. 2022, *ApJ*, 928, 188  
 Dhanpal, S., Benomar, O., Hanasoge, S., et al. 2023, *The Astrophysical Journal*, 958, 63  
 Dodd, E., Callingham, T. M., Helmi, A., et al. 2023, *A&A*, 670, L2  
 Elsworth, Y., Hekker, S., Basu, S., & R. Davies, G. 2016, *MNRAS*, 466, 3344  
 Epstein, C. R., Elsworth, Y. P., Johnson, J. A., et al. 2014, *ApJ*, 785, L28  
 Ferguson, J. W., Alexander, D. R., Allard, F., et al. 2005, *ApJ*, 623, 585  
 Fernández-Alvar, E., Kordopatis, G., Hill, V., et al. 2024, *A&A*, 685, A151  
 Formicola, A., Imbriani, G., Costantini, H., et al. 2004, *Physics Letters B*, 591, 61  
 Fox, B. 1986, *ACM Transactions on Mathematical Software*, 12, 362  
 Freytag, B., Ludwig, H. G., & Steffen, M. 1996, *A&A*, 313, 497  
 Gaia Collaboration, Prusti, T., de Bruijne, J. H. J., et al. 2016, *A&A*, 595, A1  
 Gaia Collaboration, Vallenari, A., Brown, A. G. A., et al. 2023, *A&A*, 674, A1  
 García Saravia Ortiz de Montellano, A., Hekker, S., & Themeßl, N. 2018, *MNRAS*, 476, 1470  
 Gravity Collaboration, Abuter, R., Amorim, A., et al. 2019, *A&A*, 625, L10  
 Gray, R. O. & Corbally, C. J. 1994, *AJ*, 107, 742  
 Grevesse, N. & Sauval, A. J. 1998, *Standard solar composition*  
 Grosjean, M., Dupret, M. A., Belkacem, K., et al. 2014, *A&A*, 572, A11  
 Hammer, J. W., Fey, M., Kunz, R., et al. 2005, *Nucl. Phys. A*, 758, 363  
 Handberg, R. & Campante, T. L. 2011a, *A&A*, 527, A56  
 Handberg, R. & Campante, T. L. 2011b, *A&A*, 527, A56  
 Handberg, R. & Lund, M. N. 2014, *MNRAS*, 445, 2698  
 Hekker, S. 2020, *Frontiers in Astronomy and Space Sciences*, 7, 3  
 Hekker, S. & Christensen-Dalsgaard, J. 2017, *A&A Rev.*, 25, 1  
 Hekker, S., Elsworth, Y., & Angelou, G. C. 2018, *A&A*, 610, A80  
 Helmi, A. 2020, *ARA&A*, 58, 205  
 Helmi, A., Babusiaux, C., Koppelman, H. H., et al. 2018, *Nature*, 563, 85  
 Hidalgo, S. L., Pietrinferni, A., Cassisi, S., et al. 2018, *ApJ*, 856, 125  
 Hjørringgaard, J. G., Silva Aguirre, V., White, T. R., et al. 2017, *MNRAS*, 464, 3713  
 Horta, D., Schiavon, R. P., Mackereth, J. T., et al. 2021, *MNRAS*, 500, 1385  
 Houdek, G. 2006, *arXiv e-prints*, astro  
 Huber, D., Slumstrup, D., Hon, M., et al. 2024, *arXiv e-prints*, [arXiv:2407.17566](https://arxiv.org/abs/2407.17566)  
 Hummer, D. G. & Mihalas, D. 1988, *ApJ*, 331, 794  
 Iglesias, C. A. & Rogers, F. J. 1996, *ApJ*, 464, 943  
 Jendreich, A., Weiss, A., Silva Aguirre, V., et al. 2012, *Astronomische Nachrichten*, 333, 939  
 Jiang, C. & Christensen-Dalsgaard, J. 2014, *MNRAS*, 444, 3622  
 Joe, S. & Kuo, F. 2003, *ACM Transactions on Mathematical Software*, 29, 49  
 Kallinger, T., De Ridder, J., Hekker, S., et al. 2014, *A&A*, 570, A41  
 Khan, S., Hall, O. J., Miglio, A., et al. 2018, *ApJ*, 859, 156  
 Kippenhahn, R., Weigert, A., & Weiss, A. 2013, *Stellar Structure and Evolution*  
 Kjeldsen, H. & Bedding, T. R. 1995, *A&A*, 293, 87

- Kjeldsen, H. & Bedding, T. R. 2012, in IAU Symposium, Vol. 285, *New Horizons in Time Domain Astronomy*, ed. E. Griffin, R. Hanisch, & R. Seaman, 17–22
- Kuszelewicz, J. S., Hon, M., & Huber, D. 2023, *ApJ*, 954, 152
- Lamb, H. 1932, *Hydrodynamics*, 6th edn. (Cambridge University Press)
- Larsen, J. R., Christensen-Dalsgaard, J., Lundkvist, M. S., et al. 2024, *A&A*, 690, A394
- Li, T., Bedding, T. R., Huber, D., et al. 2018, *MNRAS*, 475, 981
- Li, Y., Bedding, T. R., Li, T., et al. 2020, *MNRAS*, 495, 2363
- Lind, K., Bergemann, M., & Asplund, M. 2012, *MNRAS*, 427, 50
- Lindgren, L., Bastian, U., Biermann, M., et al. 2021, *A&A*, 649, A4
- Lindsay, C. J., Ong, J. M. J., & Basu, S. 2022, *ApJ*, 931, 116
- Lund, M. N., Silva Aguirre, V., Davies, G. R., et al. 2017, *ApJ*, 835, 172
- Mashonkina, L. et al. 2011, *Astronomy and Astrophysics*, 528, 17
- Mathur, S., Huber, D., Batalha, N. M., et al. 2017, *ApJS*, 229, 30
- Matsuno, T., Aoki, W., Casagrande, L., et al. 2021, *ApJ*, 912, 72
- McMillan, P. J. 2017, *MNRAS*, 465, 76
- Mihalas, D., Dappen, W., & Hummer, D. G. 1988, *ApJ*, 331, 815
- Mihalas, D., Hummer, D. G., Mihalas, B. W., & Daeppen, W. 1990, *ApJ*, 350, 300
- Mosser, B., Gehan, C., Belkacem, K., et al. 2018, *A&A*, 618, A109
- Mosser, B., Michel, E., Belkacem, K., et al. 2013, *A&A*, 550, A126
- Mosser, B., Pinçon, C., Belkacem, K., Takata, M., & Vrad, M. 2017, *A&A*, 600, A1
- Mosser, B., Vrad, M., Belkacem, K., Deheuvels, S., & Goupil, M. J. 2015, *A&A*, 584, A50
- Nepal, S., Chiappini, C., Queiroz, A. B., et al. 2024, *A&A*, 688, A167
- Pinçon, C., Takata, M., & Mosser, B. 2019, *A&A*, 626, A125
- Pinsonneault, M. H., Elsworth, Y., Epstein, C., et al. 2014, *ApJS*, 215, 19
- Pitrou, C., Coc, A., Uzan, J.-P., & Vangioni, E. 2018, *Phys. Rep.*, 754, 1
- Planck Collaboration, Ade, P. A. R., Aghanim, N., et al. 2016, *A&A*, 594, A13
- Rauer, H., Aerts, C., Cabrera, J., et al. 2024, arXiv e-prints, arXiv:2406.05447
- Reimers, D. 1977, *A&A*, 61, 217
- Ricker, G. R., Winn, J. N., Vanderspek, R., et al. 2014, in *Society of Photo-Optical Instrumentation Engineers (SPIE) Conference Series*, Vol. 9143, *Space Telescopes and Instrumentation 2014: Optical, Infrared, and Millimeter Wave*, ed. J. Oschmann, Jacobus M., M. Clampin, G. G. Fazio, & H. A. MacEwen, 914320
- Rogers, F. J. & Iglesias, C. A. 1992, *ApJS*, 79, 507
- Rogers, F. J. & Nayfonov, A. 2002, *ApJ*, 576, 1064
- Rogers, F. J., Swenson, F. J., & Iglesias, C. A. 1996, *ApJ*, 456, 902
- Ruchti, G. R. et al. 2011, *The Astrophysical Journal*, 743, 14
- Ruchti, G. R. et al. 2013, *Monthly Notices of the Royal Astronomical Society*, 429, 126
- Ruiz-Lara, T., Matsuno, T., Lövdal, S. S., et al. 2022, *A&A*, 665, A58
- Salaris, M., Cassisi, S., Schiavon, R. P., & Pietrinferni, A. 2018, *A&A*, 612, A68
- Schonhut-Stasik, J., Zinn, J. C., Stassun, K. G., et al. 2024, *AJ*, 167, 50
- Schönrich, R., Binney, J., & Dehnen, W. 2010, *MNRAS*, 403, 1829
- Serenelli, A., Johnson, J., Huber, D., et al. 2017, *ApJS*, 233, 23
- Sestito, F., Buck, T., Starnik, E., et al. 2021, *MNRAS*, 500, 3750
- Sestito, F., Longeard, N., Martin, N. F., et al. 2019, *MNRAS*, 484, 2166
- Silva Aguirre, V., Davies, G. R., Basu, S., et al. 2015, *MNRAS*, 452, 2127
- Slumstrup, D., Grundahl, F., Silva Aguirre, V., & Brogaard, K. 2019, *A&A*, 622, A111
- Sobol, I. 1977, *USSR Computational Mathematics and Mathematical Physics*, 16, 236
- Sobol, I. & Levithan, Y. 1976, *IPM Akademii Nauk SSSR*
- Soderblom, D. R. 2015, in *Astrophysics and Space Science Proceedings*, Vol. 39, *Asteroseismology of Stellar Populations in the Milky Way*, ed. A. Miglio, P. Eggenberger, L. Girardi, & J. Montalbán, 3
- Sotillo-Ramos, D., Bergemann, M., Friske, J. K. S., & Pillepich, A. 2023, *MNRAS*, 525, L105
- Stello, D., Chaplin, W. J., Bruntt, H., et al. 2009, *ApJ*, 700, 1589
- Stello, D., Compton, D. L., Bedding, T. R., et al. 2014, *ApJ*, 788, L10
- Stetson, P. B. & Pancino, E. 2008, *PASP*, 120, 1332
- Stokholm, A., Nissen, P. E., Silva Aguirre, V., et al. 2019, *MNRAS*, 489, 928
- Tassoul, M. 1980, *ApJS*, 43, 469
- Tayar, J., Somers, G., Pinsonneault, M. H., et al. 2017, *ApJ*, 840, 17
- Telting, J. H. et al. 2014, *Astronomische Nachrichten*, 335, 41
- Thoul, A. A., Bahcall, J. N., & Loeb, A. 1994, *ApJ*, 421, 828
- Thygesen, A. O., Frandsen, S., Bruntt, H., et al. 2012, *A&A*, 543, A160
- Viani, L. S., Basu, S., Chaplin, W. J., Davies, G. R., & Elsworth, Y. 2017, *ApJ*, 843, 11
- Vogt, S. S., Allen, S. L., Bigelow, B. C., et al. 1994, in *Society of Photo-Optical Instrumentation Engineers (SPIE) Conference Series*, Vol. 2198, *Instrumentation in Astronomy VIII*, ed. D. L. Crawford & E. R. Craine, 362
- Vrad, M., Mosser, B., & Samadi, R. 2016, *A&A*, 588, A87
- Weiss, A. & Schlattl, H. 2008, *Ap&SS*, 316, 99
- Winther, M. L., Aguirre Børsen-Koch, V., Rørsted, J. L., Stokholm, A., & Verma, K. 2023, *MNRAS*, 525, 1416
- Yu, J., Huber, D., Bedding, T. R., et al. 2018, *ApJS*, 236, 42
- Yuan, Z., Li, C., Martin, N. F., et al. 2024, *A&A*, 691, L1
- Zhou, Y., Christensen-Dalsgaard, J., Asplund, M., et al. 2024, *ApJ*, 962, 118

## Appendix A: Independent peakbagging

This appendix briefly summarises the independent peakbagging performed by the collaborators, and displays the consolidated lists of individual frequencies used in the modelling. Furthermore, Table A.1 display the available estimates for various global asteroseismic parameters obtained by the collaborators. Note that for Hennes, A16 also derived an alternate measure for the period spacing of  $\Delta\Pi_1 = 67^{+0.03}_{-0.16}$  s based on a re-formulation of mixed modes by Jiang & Christensen-Dalsgaard (2014) and implemented by Hekker et al. (2018), which does not take buoyancy glitches into account.

### Appendix A.1: Peakbagging following Li et al. 2020

We first identified oscillation modes from regular échelle diagrams for p modes as well as stretched échelle diagrams for mixed modes. Then using these initial guesses, we extracted the mode frequencies by fitting the power spectrum using a sum of Lorentzian profiles (Handberg & Campante 2011b; Davies et al. 2016). The Lorentzian profile is a typical characteristic for solar-like oscillations, as it represents an oscillation mode that experiences damping over time (Anderson et al. 1990). We followed the fitting procedure described in Li et al. (2020).

### Appendix A.2: Peakbagging with FAMED

The peakbagging analysis conducted with the FAMED pipeline (Corsaro et al. 2020) is an automated process based on the use of the public code DIAMONDS for Bayesian Inference (Corsaro & De Ridder 2014)<sup>6</sup>. The analysis builds on a preliminary step, conducted separately, which is in charge of estimating the level of the background in the stellar PDS. This preliminary phase is performed by means of the public tool DIAMONDS+BACKGROUND, which on top of estimating the model free parameters allows to identify an optimal background model, typically consisting of a series of Harvey-like profiles, a flat noise component, and a Gaussian envelope to reproduce the solar-like oscillations (Corsaro et al. 2017). The peakbagging procedure instead relies on the exploitation of a multi-modal sampling done with DIAMONDS, which quickly localizes a large number of relevant frequency peaks in the stellar PDS while ensuring the adoption of a low number of free parameters during the fitting process (Corsaro 2019).

### Appendix A.3: Peakbagging following Benomar et al. 2013

The power spectrum analysis is performed using a MCMC algorithm, initially presented in Benomar et al. (2009) and refined to fit pulsations in red giants. The multi-step approach begins by fitting a Gaussian to the mode envelope, with the noise background modelled following the formalism of Kallinger et al. (2014). The posterior distributions of the noise parameters from this initial fit are then used as priors for the detailed fit of the mode structure. A semi-automated method, relying on the Gaussian mode envelope parameters, provides the initial guesses and priors for the modes parameters, which are assumed to be symmetrical Lorentzians. Two models suitable for RGB analysis are available in the fitting software<sup>7</sup>, and we found that the most constrained model is sufficient to describe the mode pattern observed in the data. This

model closely resembles the one used by Dhanpal et al. (2022) for training machine learning models. It assumes that frequency variations of the  $\ell = 0$  and  $\ell = 2$  modes are described with a cubic spline, as in Benomar et al. 2013. However, dipole mixed modes are assumed to strictly follow the asymptotic relation for mixed modes, allowing the extraction of asymptotic parameters such as  $q$ ,  $\Delta\nu$  and  $\Delta\Pi_1$ .

For Hennes, the model accurately describes the mode patterns, with residuals of the spectrum averaging to  $\approx 1.001$  within the fitting range. Parameters show mild to no multi-modalities and are determined with high precision, as detailed in Table A.1. For Rogue, however, the posterior distribution for the period spacing is completely uniform over the range [50, 150], indicating that it is not measurable. Consequently,  $q$  peaks at a value consistent with zero are within  $2\sigma$ .

### Appendix A.4: Peakbagging with TACO

TACO, the Tools for the Automated Characterisation of Oscillations, is a data driven peakbagging code (Hekker et al. in prep.). This code aims to perform the full analysis from timeseries to fitted power density spectrum (PDS) with fully identified and characterized oscillations. The code performs a Fourier transform and fits the global features of the PDS using Bayesian methods. On the background corrected PDS, TACO automatically identifies peaks using the Mexican hat wavelet function (García Saravia Ortiz de Montellano et al. 2018). These peaks are subsequently fitted using MLE fits. As all significant peaks are fitted for, the Akaike Information Criterion (AIC) is used to identify the most significant peaks that we attribute to oscillation signals. Subsequently, TACO characterizes the fitted peaks broadly using known asymptotic relations.

### Appendix A.5: ML analysis of Hennes and Rogue

We applied a neural network, trained to infer global seismic parameters  $\Delta\nu$ ,  $\Delta\Pi$ ,  $\nu_{\max}$  and  $q$ , to the oscillation spectra of Hennes and Rogue. This convolutional neural network was trained on 5 million synthetic spectra, as described by the asymptotic theory of stellar oscillations. Additional details about the datasets and the neural network can be found in Dhanpal et al. (2022) and Dhanpal et al. (2023). Measurements on Hennes and Rogue are described in Table A.

For evolved red giants like Rogue,  $q$  is smaller ( $\approx 0.03$ ). It has been discussed in Dhanpal et al. (2023) that the uncertainty in  $\Delta\Pi$  increases at low  $q$ . This may be due to the decrease in the amplitude of g-dominated mixed modes and the reduction in the transmission factor. Consequently, this star exhibits a large uncertainty of 58 s.

### Appendix A.6: Consolidated frequencies for Hennes

The consolidated list of frequencies based on the considerations in Sect. 3.1 is displayed in Table A.2 for easy access. Note that these frequencies are the output of the peakbagging procedure of FAMED and thus the correction to the Doppler shift as proposed by Davies et al. (2014) has not been applied.

### Appendix A.7: Consolidated frequencies for Rogue

The consolidated list of frequencies based on the considerations in Sect. 3.2 is displayed in Table A.3 for easy access. Note that these frequencies are the output of the peakbagging procedure

<sup>6</sup> The public GitHub repository is available at <https://github.com/EnricoCorsaro/DIAMONDS>

<sup>7</sup> Available at <https://github.com/OthmanB/TAMCMC-C>

**Table A.1.** Estimates of the observed global asteroseismic parameters for Hennes and Rogue by A16 and other collaborators. If no uncertainty was returned, it has been left unspecified. Additionally, if an estimate of the coupling constant  $q$  was returned, it is also given.

<b>Hennes – KIC 4671239</b>				
Collaborator	$\nu_{\max}$ [ $\mu\text{Hz}$ ]	$\Delta\nu$ [ $\mu\text{Hz}$ ]	$\Delta\Pi_1$ [s]	$q$
A16	$99.2 \pm 2.5$	$9.67 \pm 0.05$	$66.0 \pm 1.0$	–
Li et al. (2020)	–	–	–	–
Corsaro et al. (2020)	99.87	9.77	62.3	–
Benomar et al. (2013)r	–	$9.798 \pm 0.001$	$66.53 \pm 0.01$	$0.27 \pm 0.02$
Dhanpal et al. (2023)	$105.6 \pm 1.1$	$9.83 \pm 0.05$	$66.4 \pm 1.2$	$0.26 \pm 0.03$
<b>Rogue – KIC 7693833</b>				
Independent Determination	$\nu_{\max}$ ( $\mu\text{Hz}$ )	$\Delta\nu$ ( $\mu\text{Hz}$ )	$\Delta\Pi_1$ (s)	$q$
A16	$31.8 \pm 1.0$	$4.03 \pm 0.05$	$56.6 \pm 2$	–
Li et al. (2020)	–	–	–	–
Corsaro et al. (2020)	32.35	4.06	–	–
Benomar et al. (2013)	–	4.10	$105.2 \pm 28.0$	$0.09 \pm 0.07$
Dhanpal et al. (2023)	$33.2 \pm 2$	$4.04 \pm 0.035$	$61.3 \pm 58.1$	$0.03 \pm 0.02$

described in A.1 and thus the correction to the Doppler shift as proposed by Davies et al. (2014) has not been applied.

**Table A.2.** Consolidated list of individual frequencies for Hennes. No correction to the Doppler shift has been applied.

<b>Hennes – KIC 4671239</b>			
Order $n$	Degree $\ell$	Frequency [ $\mu$ Hz]	Uncertainty [ $\mu$ Hz]
5	2	68.1678	0.2135
6	0	69.5850	0.0808
6	1	74.2323	0.0757
6	1	74.5773	0.0459
6	2	77.2774	0.0539
7	0	78.7856	0.0628
7	1	82.9593	0.0938
7	1	83.5408	0.0670
7	1	84.2097	0.0974
7	1	85.1689	0.0350
7	2	86.9481	0.1888
8	0	88.5026	0.0946
8	1	92.4132	0.1938
8	1	92.9687	0.0798
8	1	93.5001	0.1104
8	1	93.9274	0.0956
8	1	94.5140	0.1539
8	2	96.6655	0.1482
9	0	98.1491	0.1165
9	1	100.8280	0.0619
9	1	101.5738	0.1190
9	1	102.3327	0.0391
9	1	102.8020	0.0493
9	1	103.4309	0.0602
9	1	104.0100	0.0403
9	1	104.6220	0.0500
9	1	105.3686	0.0709
9	2	106.5278	0.1898
10	0	108.0101	0.1496
10	1	111.4051	0.0215
10	1	112.1443	0.0331
10	1	112.8324	0.0423
10	1	113.5163	0.0414
10	1	114.2211	0.0713
10	1	115.0487	0.0568
10	2	116.5503	0.1358
11	0	118.0876	0.1260
11	1	122.3061	0.0617
11	1	123.0262	0.0528
11	1	123.6331	0.0264
11	2	126.4318	0.1612
12	0	128.0299	0.0696
12	1	133.1081	0.0117
12	1	133.9477	0.0455

**Table A.3.** Consolidated list of individual frequencies for Rogue. No correction to the Doppler shift has been applied.

<b>Rogue – KIC 7693833</b>			
Order $n$	Degree $\ell$	Frequency [ $\mu$ Hz]	Uncertainty [ $\mu$ Hz]
3	2	19.3921	0.0492
4	0	20.2413	0.0304
4	1	22.3579	0.0406
5	2	23.4145	0.0196
5	0	24.0470	0.0146
5	1	26.0382	0.0316
6	2	27.2797	0.0160
6	0	27.9256	0.0102
6	1	30.0742	0.0483
7	2	31.3467	0.0131
7	0	31.9625	0.0096
7	1	34.0882	0.0438
8	2	35.3831	0.0328
8	0	36.0381	0.0143
8	1	38.3250	0.0401
9	2	39.6462	0.0607
9	0	40.2443	0.0536

## Appendix B: Corner plots of modelling results

This appendix displays the corner plots of the posterior distributions obtained from the grid-based stellar modelling of Hennes and Rogue in Figures B.1 and B.2. The corner plots show each of the stellar parameters displayed in Tables 4 and 5 plotted against one another. This allows for visual inspection of correlations between the parameter dimensions. The marginalised posterior distribution of each parameter is showed on the top of their respective column, indicating the median (solid line) and 16th and 84th percentiles (dashed lines), which we will use as central value and uncertainties in this work.

Uniquely for the modelling of Rogue, we allowed the values of the mixing length parameter  $\alpha_{\text{mlt}}$  and initial helium abundance  $Y_{\text{ini}}$  to vary freely. From the posteriors obtained for Rogue, we extracted the obtained values of these parameters to be  $\alpha_{\text{mlt}} = 1.893^{+0.069}_{-0.050}$  and  $Y_{\text{ini}} = 0.251^{+0.005}_{-0.002}$ . These values do not strongly deviate from expectations, as the mixing length is close to our solar calibrated value of  $\alpha_{\text{mlt}} = 1.786$  and the initial helium is in coherence with the estimates from a chemical enrichment law  $dY/dZ = 1.4$ .

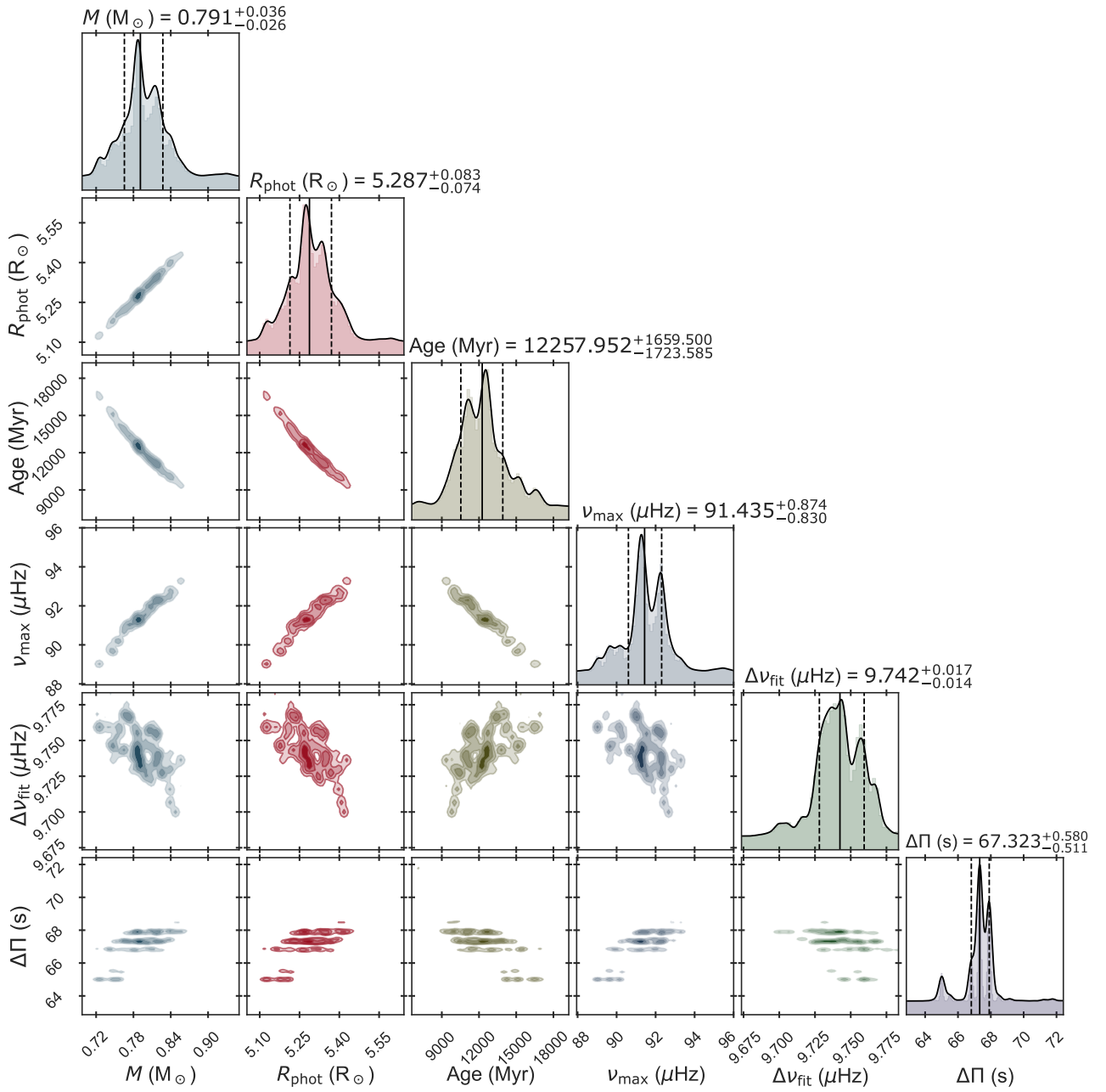


**Fig. B.1.** Corner plot showing the posterior distributions obtained for the fundamental stellar parameters and global asteroseismic parameters of Hennes.

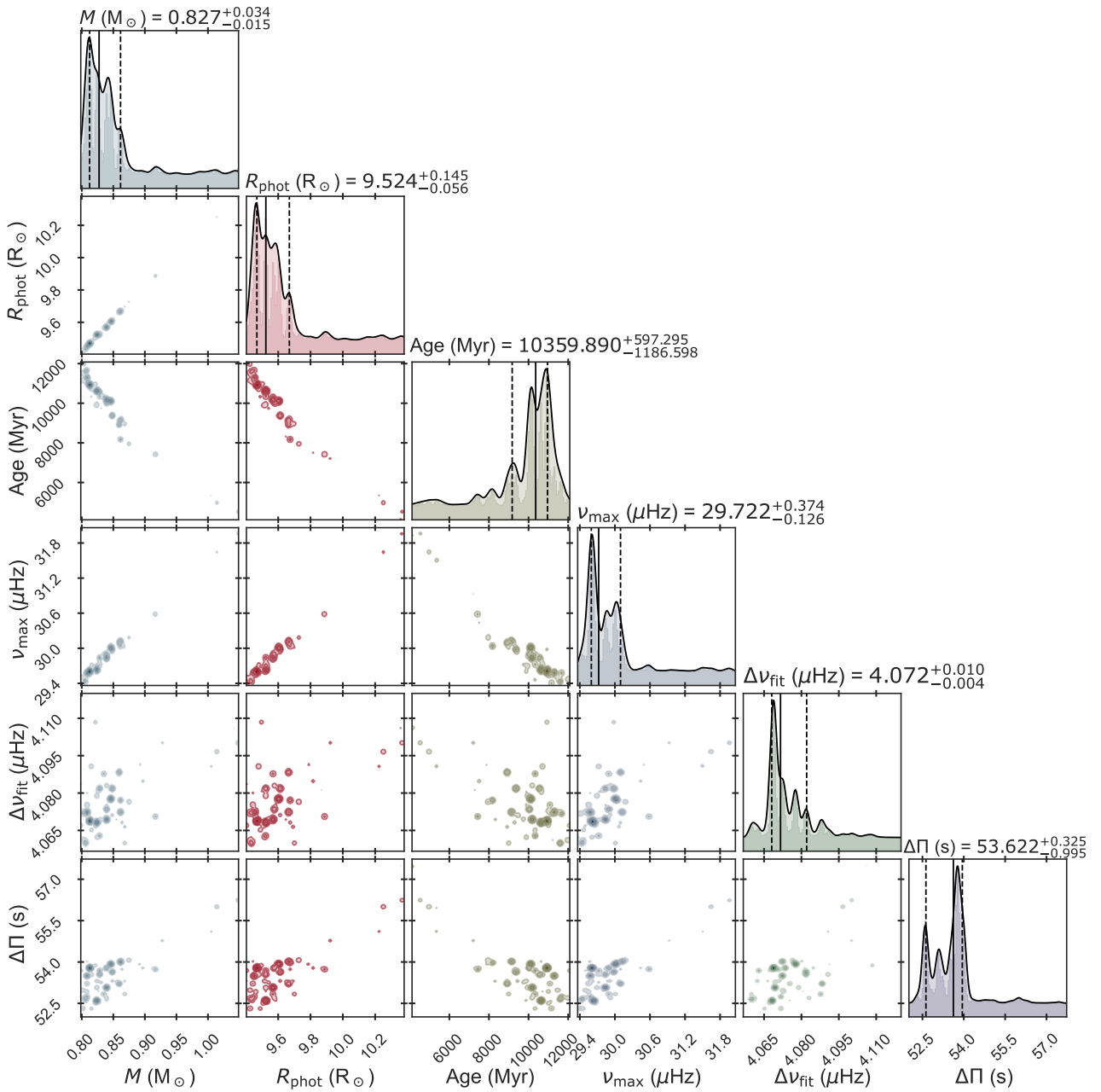


**Fig. B.2.** Corner plot displaying the posteriors obtained for the fundamental stellar parameters and global asteroseismic parameters from the modelling of Rogue.

### Appendix C: Fitting the global asteroseismic parameters

**Table C.1.** Modelling results for Hennes when using global asteroseismic parameters. All stellar parameters are given by the median of the posterior distribution, with uncertainties as the 16th and 84th quantiles.

Hennes – KIC 4671239			
Stellar parameter	This work	A16	Alencastro Puls et al. 2022
$M [M_{\odot}]$	$0.87^{+0.02}_{-0.02}$	$1.00^{+0.10}_{-0.08}$	$1.01^{+0.02}_{-0.02}$
$R [R_{\odot}]$	$5.46^{+0.05}_{-0.06}$	$5.73^{+0.19}_{-0.17}$	$5.70^{+0.05}_{-0.05}$
Age [Gyr]	$8.7^{+0.8}_{-0.7}$	$5.28^{+1.90}_{-1.48}$	$5.4^{+0.4}_{-0.3}$
$\nu_{\max} [\mu\text{Hz}]$	$94.36^{+0.73}_{-0.74}$	–	–
$\Delta\nu [\mu\text{Hz}]$	$9.85^{+0.05}_{-0.04}$	–	–
$\Delta\Pi_1 [s]$	$69.10^{+0.97}_{-0.94}$	–	–

In order to emphasise the contrast to the previously best-possible case when asteroseismically modelling giant stars, we here present the results from a fit to the global asteroseismic parameters  $\Delta\nu$ ,  $\nu_{\max}$  and  $\Delta\Pi_1$ . The same classical parameters as in Sect. 5 are included in the fit. For Rogue, due to the reasons described in Sect. 3.2, we do not attempt to fit  $\Delta\Pi_1$ .

Figures C.1 and C.2 show the Kiel diagrams for Hennes and Rogue, respectively. A clear lack of overlap between the observed constraint bands are seen, i.e. a tension between the observables when translated to model space. This was the same situation that A16 initially faced when performing the modelling attempts ten years ago. Tables C.1 and C.2 show the stellar parameters obtained for the modelling. Both Hennes and Rogue are recovered as vastly different stars from the ones found by modelling them utilising individual frequencies (see Sect 5). Note that the lower uncertainties recovered here, when compared to the ones found by the individual frequency modelling, occur due to the low uncertainties on the global asteroseismic parameters and the lacking overlap between them in model space.

A final interesting mention is that when we fit the global asteroseismic parameters but omit  $\nu_{\max}$ , we can generally recover an overlap between the fitted constraints. This provides posteriors much more similar to the ones from individual frequency modelling. The posteriors are wider, which results in larger errors on the determined parameters, but encompasses the solution found by the individual frequency modelling. This further speaks to the unreliability of the  $\nu_{\max}$  scaling relation for low-metallicity evolved stars (see Sect. 6.2).

### Appendix D: Orbital Solutions for Hennes and Rogue

Table D.1 lists the orbital properties for Hennes and Rogue as described in Sect. 6. *GC* refers to Galactocentric quantities, while *HC* are heliocentric.

**Table C.2.** Modelling results for Rogue when using global asteroseismic parameters. All stellar parameters are given by the median of the posterior distribution, with uncertainties as the 16th and 84th quantiles.

Rogue – KIC 7693833		
Stellar parameter	This work	A16
$M [M_{\odot}]$	$1.04^{+0.006}_{-0.003}$	$0.97^{+0.12}_{-0.10}$
$R [R_{\odot}]$	$10.56^{+0.03}_{-0.03}$	$10.03^{+0.48}_{-0.42}$
Age [Gyr]	$4.81^{+0.05}_{-0.14}$	$6.29^{+3.19}_{-2.20}$
$\nu_{\max} [\mu\text{Hz}]$	$30.83^{+0.09}_{-0.05}$	–
$\Delta\nu [\mu\text{Hz}]$	$4.02^{+0.02}_{-0.01}$	–
$\Delta\Pi_1 [s]$	$56.11^{+0.32}_{-0.39}$	–

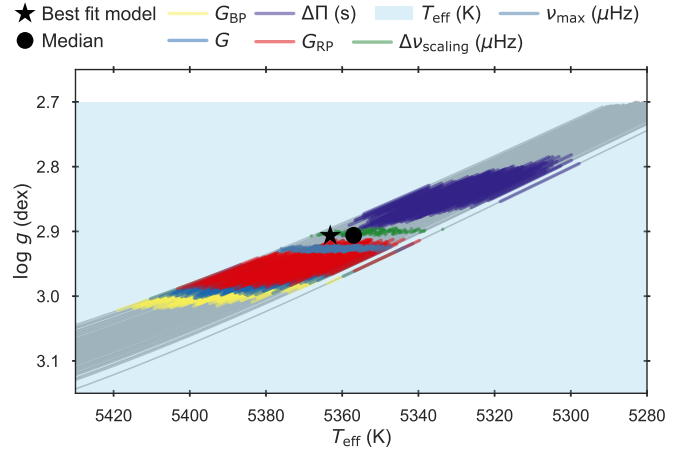


**Fig. C.1.** Kiel diagram of Hennes for a fit to the global asteroseismic parameters, displaying a representative number of stellar tracks in the grid. The observed constraints on the fitted parameters are overlaid to show a clear lack of overlap with the median and BFM from the posterior.

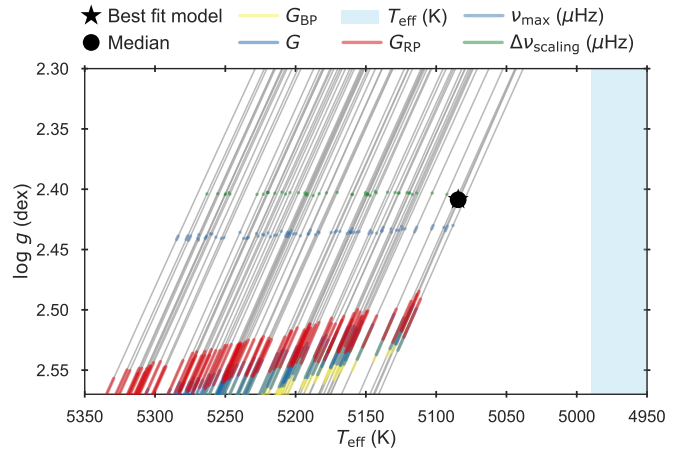


**Fig. C.2.** Kiel diagram of Rogue for a fit to the global asteroseismic parameters, displaying a representative number of stellar tracks in the grid. The observed constraints on the fitted parameters are overlaid to show a clear lack of overlap with the median and BFM from the posterior.

Table D.1.

Orbital parameter	Hennes – KIC 4671239	Rogue – KIC 7693833
$X$ (GC) (kpc)	$7.85^{0.01}_{0.01}$	$7.59^{0.02}_{0.01}$
$Y$ (GC) (kpc)	$1.54^{0.02}_{0.03}$	$2.13^{0.05}_{0.06}$
$Z$ (GC) (kpc)	$0.3^{0.0}_{0.0}$	$0.33^{0.01}_{0.01}$
$U$ (HC) (km/s)	$-26.0^{0.4}_{0.4}$	$-87.4^{1.3}_{1.0}$
$V$ (HC) (km/s)	$0.4^{0.2}_{0.2}$	$-191.6^{1.9}_{1.3}$
$W$ (HC) (km/s)	$-8.9^{0.3}_{0.1}$	$118.4^{3.0}_{4.2}$
$R$ (GC) (kpc)	$7.999^{0.001}_{0.001}$	$7.883^{0.001}_{0.0}$
$\phi$ (GC) (kpc)	$2.95^{0.0}_{0.0}$	$2.87^{0.01}_{0.01}$
$Z$ (GC) (kpc)	$0.3^{0.0}_{0.0}$	$0.33^{0.01}_{0.01}$
$v_R$ (GC) (km/s)	$59.6^{1.0}_{1.3}$	$84.5^{0.7}_{1.1}$
$v_\phi$ (GC) (km/s)	$226.3^{0.4}_{0.3}$	$19.6^{1.9}_{2.2}$
$v_z$ (GC) (km/s)	$-1.6^{0.3}_{0.1}$	$125.9^{3.0}_{4.2}$
$J_R$ (km/s kpc)	$51^{1}_{2}$	$503^{9}_{3}$
$L_z$ (km/s kpc)	$1864.7^{3.8}_{2.6}$	$159.0^{23.7}_{17.7}$
$J_z$ (km/s kpc)	$3.0^{0.1}_{0.1}$	$352.2^{28.4}_{32.4}$
$e$ (–)	$0.194^{0.003}_{0.004}$	$0.909^{0.009}_{0.013}$
$z_{\max}$ (kpc)	$0.38^{0.001}_{0.001}$	$6.67^{0.04}_{0.05}$
$r_{\text{peri}}$ (kpc)	$7.057^{0.003}_{0.004}$	$0.445^{0.008}_{0.005}$
$r_{\text{ap}}$ (kpc)	$10.45^{0.002}_{0.008}$	$9.366^{0.008}_{0.01}$
Energy ((km/s) <sup>2</sup> )	$-157510^{61}_{60}$	$-173911^{373}_{669}$
$L_{\text{total}}$ (km/s kpc)	$1811^{4}_{2}$	$980^{18}_{35}$